*Review*

# Non-Metal-Doped Porous Carbon Nitride Nanostructures for Photocatalytic Green Hydrogen Production

Qingqing Lu [1], Ahmed Abdelgawad [2], Jiaojiao Li [1] and Kamel Eid [2],*

[1] Engineering & Technology Center of Electrochemistry, School of Chemistry and Chemical Engineering, Qilu University of Technology (Shandong Academy of Sciences), Jinan 250353, China
[2] Gas Processing Center (GPC), College of Engineering, Qatar University, Doha 2713, Qatar
* Correspondence: kamel.eid@qu.edu.qa

**Abstract:** Photocatalytic green hydrogen ($H_2$) production through water electrolysis is deemed as green, efficient, and renewable fuel or energy carrier due to its great energy density and zero greenhouse emissions. However, developing efficient and low-cost noble-metal-free photocatalysts remains one of the daunting challenges in low-cost $H_2$ production. Porous graphitic carbon nitride (gCN) nanostructures have drawn broad multidisciplinary attention as metal-free photocatalysts in the arena of $H_2$ production and other environmental remediation. This is due to their impressive catalytic/photocatalytic properties (i.e., high surface area, narrow bandgap, and visible light absorption), unique physicochemical durability, tunable electronic properties, and feasibility to synthesize in high yield from inexpensive and earth-abundant resources. The physicochemical and photocatalytic properties of porous gCNs can be easily optimized via the integration of earth-abundant heteroatoms. Although there are various reviews on porous gCN-based photocatalysts for various applications, to the best of our knowledge, there are no reviews on heteroatom-doped porous gCN nanostructures for the photocatalytic $H_2$ evolution reaction (HER). It is essential to provide timely updates in this research area to highlight the research related to fabrication of novel gCNs for large-scale applications and address the current barriers in this field. This review emphasizes a panorama of recent advances in the rational design of heteroatom (i.e., P, O, S, N, and B)-doped porous gCN nanostructures including mono, binary, and ternary dopants for photocatalytic HERs and their optimized parameters. This is in addition to $H_2$ energy storage, non-metal configuration, HER fundamental, mechanism, and calculations. This review is expected to inspire a new research entryway to the fabrication of porous gCN-based photocatalysts with ameliorated activity and durability for practical $H_2$ production.

**Keywords:** porous $C_3N_4$; carbon nitride; heteroatom-doped; non-metal-doped; hydrogen evolution reaction; photocatalysts; water slitting; green hydrogen production

## 1. Introduction

The inevitable overuse of fossil fuels (i.e., crude oil, natural gas, and hard coal) generate massive greenhouse gas emissions which are the main contributors to global warming and climate change and increased energy crisis [1,2]. Ceaseless efforts dedicated to defeating this issue have culminated in the conversion of gas to useful chemicals [3–6] and the development of green energy resources such as biofuel [7] and fuel cells (i.e., methanol [8,9], ethanol [10], glucose [11], oxygen evolution [10], oxygen reduction [12,13]). Hydrogen ($H_2$) is one of the most promising green, renewable, and carbon-free fuel or energy carriers, owing to its impressive energy content, earth-abundant resources (i.e., alcohols, methane, and water), and zero greenhouse gas emission [14,15]. $H_2$ is produced through various processes such natural gas reformation [16,17], biological (i.e., bacteria and microalgae), biomass, and solar (i.e., photobiological, photoelectrochemical, and solar thermochemical) [18–21]. Unlike these methods, the green $H_2$ evolution reaction (HER) through water electrolysis driven by electrocatalysts (i.e., Pt, Pd, Ru, and Ir), photocatalysts (i.e., metal

oxides, metal nitrides, and metal sulfides), and their composites is more promising [22–25]. Notably, noble metals or Pt-group elements remain the most active catalysts for HERs; however, their earth scarcity and high cost are critical barriers in low-cost HERs [23].

Distinct from noble metals, porous carbon nitride (gCN) nanostructures are physicochemically durable (i.e., thermally stable up to 600 °C, chemically stable in different solvents, and mechanically robust) and, most importantly, are easily synthesized at large scale from cheap and earth-abundant nitrogen-rich organic precursors (i.e., urea, melamine, thiourea, and cyanamide), most of which are produced as byproducts of various industrial processes [26–31]. The landmark event of a photocatalytic HER on gCN materials was ignited by the pioneering work conducted by Wang et al. in 2009, which showed the $H_2$ production of 7.6 µmol on bare gCNs and increased loaded Pt nanoparticles (15 µmol) via the addition of Pt after 72 h [32]. This study opened new vistas for rational design and utilization of gCNs as photocatalysts for HERs and other applications. Porous gCNs are semiconductors with a bandgap of nearly 2.7 eV and high adsorption of blue-violet light with a wavelength of (<475 nm) that accelerate the migration of photogenerated electrons along with delayed electron–hole recombination [26–31]. Moreover, porous gCNs possess high surface area, low density, rich electron density, and massive active sites, which can accelerate the reaction kinetics and maximize the utilization of elements during HER [33–35]. The physiochemical and photocatalytic properties of gCNs are easily modulated via the incorporation of metal or non-metal elements to form various heterojunction structures of Z-Scheme, Type-II, and S-Scheme [33–37]. Heteroatoms (i.e., B, S, O, F, and P) are easily integrated into the skeleton structure of gCNs to optimize their electronic structure, bandgap energy, visible-light absorption, and photocatalytic properties [35,38,39]. Also, Heteroatoms are inexpensive, earth-abundant, and easily handled or stored, which makes them feasible or practical applications [40].

There have been sensible accumulative efforts in the last decade for the fabrication of porous gCN photocatalysts for $H_2$ production, which led to 882 published articles, including 424 articles on doped porous gCN and only 93 articles on heteroatom-doped porous gCNs for $H_2$ production (Figure 1a). Therefore, it is essential to provide timely updates in this research area to highlight the research related to fabrication of novel gCNs for large-scale applications and address the current barriers in this field. There are various reviews on porous gCN-based photocatalysts for various applications (Table 1); however, to the best of our knowledge, there are no reviews on heteroatom-doped porous gCN nanostructures for the photocatalytic $H_2$ production reaction.
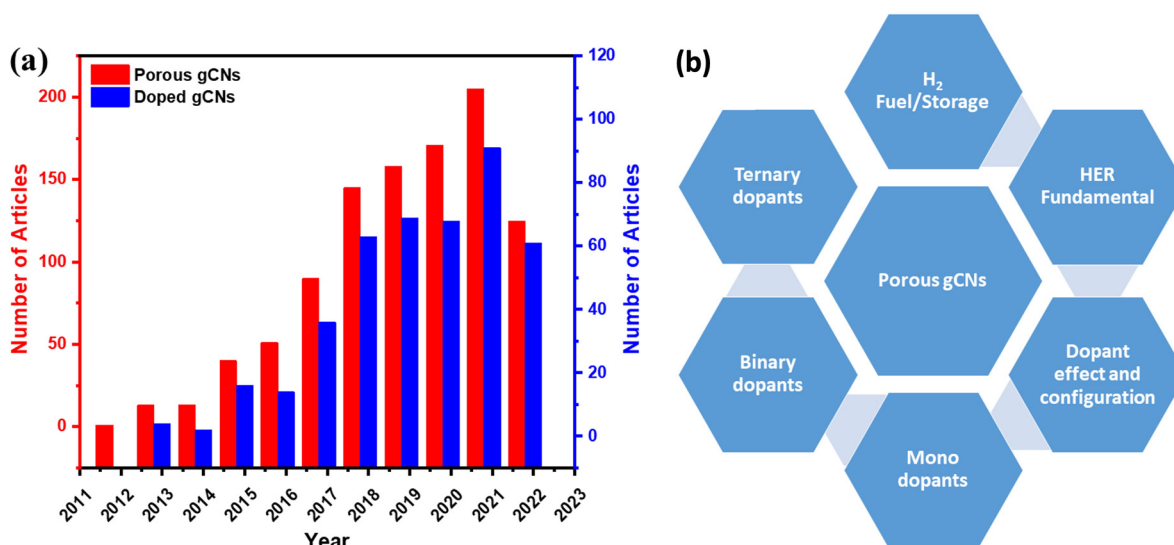


**Figure 1.** (**a**) The articles related to porous gCNs and doped gCNs published between 2012 and 18 October 2022, obtained from Web of Science data. (**b**) The overall focus of this review.

**Table 1.** Summary of the main reviews related to porous heteroatom-doped porous carbon nitride-based nanostructures for photocatalytic HER compared in the present review.

| Title | Focus | Ref. |
|---|---|---|
| Non-metal-Doped Porous Carbon Nitride Nanostructures for Photocatalytic Green Hydrogen Production | Rational design of heteroatoms (i.e., B, N, S, P, F, and O) doped porous carbon nitride for the photocatalytic HER. The effect of mono, binary, and ternary dopants on photocatalytic HER, and their fundamentals and mechanisms are discussed. $H_2$ energy and storage in addition to HER fundamentals and calculation are also discussed. The current challenges and possible solutions for the synthesis of active gCN photocatalysts for green HERs are also emphasized. | This work |
| Photocatalytic hydrogen evolution based on carbon nitride and organic semiconductors | Organic (i.e., carbon nitride, linear polymers, conjugated porous polymers, and small molecules) for a photocatalytic HER. | [33] |
| Solvent-Assisted Synthesis of Supramolecular-Assembled Graphitic Carbon Nitride for Visible Light Induced Hydrogen Evolution—A Review | Solvent (i.e., water, DMSO, and water–chloroform) assisted the supramolecular-assembled carbon nitride via hydrogen bonding and hydrogen–halogen interaction. This is in addition to tunable characteristics/properties of photocatalytic HERs. | [34] |
| A latest overview on photocatalytic application of g-$C_3N_4$ based nanostructured materials for hydrogen production | g-$C_3N_4$ nanosheets supported metals (i.e., transition metals, non-metals, noble, and semiconductor), and carbon materials (i.e., graphene and carbon nanotubes, and carbon dots) for photocatalytic HER. | [35] |
| Preparation, Physicochemical Properties, and Functional Characteristics of Carbon Nitride: a Review | Emphasizing various approaches for preparation, and functionalization of porous carbon nitride and their properties that could enhance the photocatalysis, catalysis, and adsorption applications. | [41] |
| g$C_3N_4$ Derived Materials for Photocatalytic Hydrogen Production: A Mini Review on Design Strategies | Highlighting the recent advance in doped g-$C_3N_4$ with metals/non-metals (i.e., Ag, Ni, Mo, F, B, and S) and formation of heterojunction with semiconductors (i.e., $TiO_2$, ZnO, $MCoS_2$), metal-organic framework, graphdiyne for photocatalytic HERs, and their mechanisms. | [38] |
| Latest progress in g-$C_3N_4$ based heterojunctions for hydrogen production via photocatalytic water splitting: a mini review | The fabrication of g-$C_3N_4$-based heterojunctions (i.e., type-II, Z-scheme, S-scheme and Schottky) with transition metal oxide/sulfide (i.e., $Co_2P$, FeOx, CuS, $Cu_2O$, Ni) noble-metals (i.e., Ag, Au, Pt, and Pd), non-metals (i.e., B, F, S, and W), semiconductors (ZnO, $ZrO_2$, and $Mo_2S$), and carbon materials (graphene, carbon, nanotubes, and carbon dots) for photocatalytic HERs. | [36] |
| 2D Graphitic Carbon Nitride for Energy Conversion and Storage | The preparation (i.e., thermal oxidation etching, chemical exfoliation, ultrasonication-assisted liquid phase exfoliation, chemical vapor deposition) of energy production (i.e., photo-/electrocatalytic HER, $CO_2$ reduction, and oxygen evolution/reduction) and energy storage (i.e., alkali-metal ion, lithium-metal, lithium-sulfur batteries, metal-air batteries, and supercapacitors). | [42] |
| Recent advances on porous materials for synergetic adsorption and photocatalysis | Focus on the fabrication of porous g-$C_3N_4$, metal oxides/sulfides (i.e., ZnS, $SnS_2$, $BiS_3$), metal-organic frameworks (i.e., ZIF, MIL, and PCN) for photocatalytic HERs, and photocatalytic adsorbents ($TiO_2$-actvated carbon, activated carbon-$MoS_2$, and biochar-$TiO_2$). | [37] |
| Co-Doped, Tri-Doped, and Rare-Earth-Doped g-$C_3N_4$ for Photocatalytic Applications: State-of-the-Art | Unravelling the effects of co-doping, tri-doping, and rare-earth-doping of g-$C_3N_4$ with non-metals (i.e., P, F, N, I, S, Cl) and metals (Ag, Fe, Co, and Pt) on photocatalytic water splitting and dye degradation. | [39] |
| Recent advances in g-$C_3N_4$-based photocatalysts incorporated by MXenes and their derivatives | The fabrication of g-$C_3N_4$/2D MXenes (I.e., $Ti_3C_2T_x$, $Nb_2CT_x$) and their derivatives for environmental and energy applications (i.e., photocatalytic HER, generation, $CO_2$ conversion, pollutant degradation, $N_2$ fixation, and $H_2O_2$ production). | [43] |

This review presents the controlled fabrication of porous gCN nanostructures functionalized with mono, binary, and ternary heteroatoms (i.e., P, O, S, N, and B) for photocatalytic

$H_2$ production. This includes tailoring the physiochemical and photocatalytic merits of porous gCN nanostructures and their photocatalytic $H_2$ production activity and durability in addition to dissuasion on the optimization of photocatalytic $H_2$ production as a function of catalyst shape, composition, bandgap, and electrolyte type/concentration.

*Novelty and Focus Review*

Table 1 shows the focus of the published reviews related to gCN-based nanostructures for $H_2$ production compared with our present review. It is obvious that previous reviews focused on gCN fabrication strategies for photocatalytic $H_2$ production or other applications. This is in addition to the formation of heterojunctions structures (Z-scheme, S-scheme, and Type-II scheme) via coupling with other semiconductors (i.e., metal oxides and metal sulfides), carbon materials (i.e., graphene, metal-organic framework, and graphdiyne), and metals/non-metals elements (i.e., Pt, Ag, Ni, Mo, F, and B) for photocatalytic $H_2$ production and other applications as well. In this review, we collected all the articles related to heteroatom-doped porous gCN nanostructures for $H_2$ production from the Web of Science, Scopus, and Scifinder databases without bias. Distinct from previous reviews, the main foci of this review are summarized in Table 1, which includes (1) the fundamentals of water electrolysis; (2) the rational design of porous gCN nanostructures functionalized with mono, binary, and ternary heteroatoms (i.e., P, O, S, N, and B) and exploitation of their unique photocatalytic $H_2$ production properties; (3) $H_2$ energy and storage; (4) HER fundamental and calculation; (5) discussion on the optimization of the photocatalytic $H_2$ production and (6) current challenges facing and future remarks on directing the synthesis of porous gCNs for practical applications (Figure 1b).

## 2. $H_2$ as Fuel Strategy

The demand for $H_2$ increased by nearly three times in the last 3 decades and is expected to continue to rise to reach the net carbon-free emissions target by 2050. The earth resources for $H_2$ are plentiful, including $H_2O$ and hydrocarbons (i.e., $CH_4$), and it is easily extracted from fossil fuels (i.e., crude oil, natural gas, and hard coals), biomass, and water [18–21]. Currently, natural gas is the main source of $H_2$ production (~95%), which not only consumes almost 6% of global natural gas and 2% for production of 70 million tons annually, but also generates a huge amount of $CO_2$ emissions [44,45]. Mainly, $H_2$ production—from crude oil or hydrocarbons—allows complete formation from carbon to $CO_2$, while considering the energy for combustion each 1 million SCF of $H_2$ produces 19.3 metric tons of $CO_2$.

$H_2$ fuel is green and effective, with outstanding energy compared to traditional sources. $H_2$ has the greatest energy per mass of any other fuel. For example, 1 kg $H_2$ produces 120 MJ of energy, which is equivalent to 1 gallon of gasoline (44 mJ/kg) and provides 9.1 kg of $CO_2$ after combustion [14,15]. However, $H_2$, due to its inferior ambient temperature density, has a low energy per unit volume. Even in liquid form, $H_2$ has an energy density of 8 MJ/L compared to gasoline (32 MJ/L) [14,15]. Thus, $H_2$ requires the rational design of an efficient storage system with potential for greater energy density. $H_2$ is stored physically as either gas in high-pressure tanks at 350–700 bar or as a liquid that needs cryogenic temperatures owing to the negative boiling point of $H_2$ (−252.8 °C) at one-atmosphere pressure [18,46–48]. $H_2$ can also be stored via the adsorption on the surfaces of adsorbents (i.e., MOF, liquid organic, interstitial hydride, complex hydride, and chemical hydrogen) (Figure 2) [18,46–48]. $LiBH_4$-based materials are one of the promising materials for hydrogen storage/release [49–54]. However, the thermodynamics and sluggish kinetics of hydrogenation/dehydrogenation is a major obstacle in hydrogen storage/release. Research efforts to improve the hydrogenation/dehydrogenation of this material have utilized multiple approaches. Notably, nanoengineering through techniques like ball milling and confinement in a nanoporous scaffold can reduce grain size and particle size as well as increase the number of defects to allow better diffusion of $H_2$ and thereby enhanced kinetics of $H_2$ adsorption/desorption. Another strategy to improve the kinetics of $H_2$

adsorption/desorption is to dope $LiBH_4$ with metals such as Ti, metal oxides such as $SiO_2$ and $TiO_2$, and halides such as $TiCl_3$. However, the effect of doping is almost negligible on hydrogen re-absorption [50]. Moreover, tuning the thermodynamics of $LiBH_4$ can allow for better hydrogen adsorption or desorption [49,53]. This can be achieved through partial substitution of the metal cation with metals of a lower electronegativity or the $BH_4$ anion by elements such as F to yield more thermodynamically favorable adsorption/desorption. Notably, hybrid materials made of $Mg(BH_4)$, $LiBH_4$, and $MgH_2$ using a novel fabrication technique has shown to be promising for hydrogen storage/release: 5 wt% in solid state at temperatures <265 °C [49–56]. The hybrid mix is fabricated using room temperature ball milling of $MgH_2$ with in situ aerosol spraying of $LiBH_4$. In addition to experimental efforts, machine learning was employed to predict the hydrogen release ability of $LiBH_4$ materials and the rank of major variables including sample preparation, mixing conditions, and operational variables [49]. In spite of research efforts to develop and optimize materials for hydrogen storage, the capacity for hydrogen storage is currently very limited and requires high temperatures, which makes it energetically unfavorable. However, further investigations are still needed to develop new storage methods for tanks for more effect delivery and to avoid current challenges. $H_2$ density shortage remains a daunting challenge for transportation applications, as it needs huge volume systems in gaseous form, so fuel-cell-powered vehicles contain compressed gas onboard storage with large-volume and high-pressure composite vessels that can withstand driving for more than 300 miles and can accommodate large $H_2$ storage capacity (5–13 kg) onboard [14,15,18,46–48].
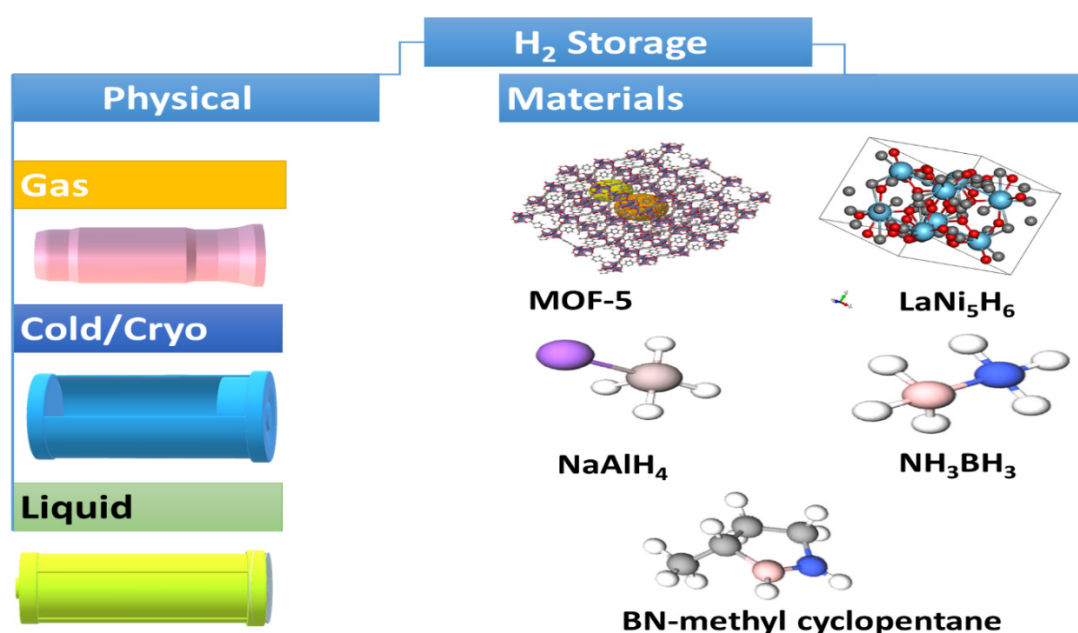


**Figure 2.** The main $H_2$ storage methods.

*Solar-Driven $H_2$ Production*

The utilization of solar energy in green $H_2$ production could be carried out through two main approaches including water electrolysis using solar-generated electricity and direct solar water splitting [18–21]. However, the solar-driven electricity "photovoltaic-electrolysis-fuel cell" should soon be available to make solar-driven $H_2$ production a feasible process, which is not possible in remote areas or during seasonal variations.

Photovoltaic electrolysis-driven $H_2$ production, especially for automobile applications, is not feasible supposing the fueling station needs nearly 1000 kg $H_2$/day and considering that the minimal electrical energy required for production of 1kg $H_2$ is 51 kWh (utilizing an electrolyzer efficiency of 65%) [33–40]. Thereby, 1000 kg $H_2$/day needs 51,000 kWh/day of

electricity that requires operation of 10,200 kWp or 10.2 megawatts of PV power. Notably, 1 kWp needs about 10 m$^2$ area for PV at 10% efficiency.

Direct solar $H_2O$ splitting entails the direct utilization of solar energy in the production of $H_2$ from water without going through intermediate electrolysis, which includes the following concepts [33–40]:

- Photoelectrochemical $H_2O$ splitting driven by quantum dots or semiconductor (i.e., electrodes using a photoelectrochemical cell) to convert light energy into $H_2$ chemical energy. Photoelectrochemical systems could be based on semiconductors or dyes and using dissolved metal complexes.
- The photobiological process includes the production of $H_2$ from biological systems (i.e., algae and bacteria using sunlight driven by the initial absorption of light by the pigments in algae while the enzymes in the cell act as catalysts to promote $H_2$ or $O_2$ production). Both photoelectrochemical and photobiological approaches should be improved significantly to meet large-scale applications because current solar-to-$H_2$ systems' efficiencies are less than 1%.
- Thermochemical cycles for generating high temperature from solar light to produce $H_2$, which can achieve efficiencies higher than 40%. However, it needs a concentrated solar receiver/reactors able to generate a high temperature of nearly 800 °C.

According to the US department of energy, photocatalytic water electrolysis is the main pathway for $H_2$ production to reach the $H_2$ energy earth-shot aim of decreasing the cost of $H_2$ by 80% to nearly 1 USD/kg along with zero greenhouse gas emissions by 2031 [57–59]. In spite of the great progress made in photocatalytic HERs, the current efficiency is not up to a level that meets practical requirements. In particular, considering daily sunlight illumination (AM 1.5 G) of 7.6 h (assigned to 240 W/m$^2$), to reach a hydrogen price of 3.5 USD/kg, it is estimated that a HER system with an STH of (10%), lifetime of (10 years), decreasing rate of 4%/year, and subsequent acceptable cost of 102 USD/m$^2$ is required. Therefore, further efforts including both experimental and theoretical studies along with fundamental investigations are needed to develop efficient and low-cost photocatalysts for large-scale photocatalytic HER processes [33–40].

## 3. Fundamentals of HER

### 3.1. Photocatalytic HER Mechanism

The photocatalytic water-splitting reaction on gCN to produce $H_2$ comprises three consequent main steps as follows [33–40].

The initial absorption of photons when photon energy is $\geq$ than the bandgap of gCN to generate electron–hole pairs (e$^-$/h$^+$) via the excitation of electrons from the valence band (VB) to the conduction band (CB) while the holes are left in the VB:

(I) The isolation of the photoexcited carriers into free carriers followed by migration to the active sites of gCN.

(II) The initiation of a reduction reaction comprising these charges to produce $H_2$ on the surface of gCN with the assistance of e$^-$ in the CB. The HER reaction in different electrolytes is shown in Equations (1) and (2)

In an aqueous solution of acidic electrolyte

$$2H^+ + 2e^- \rightarrow H_2 \tag{1}$$

In an aqueous solution of alkaline electrolyte

$$2H_2O + 2e^- \rightarrow H_2 + 2OH^- \tag{2}$$

The overall solar HER efficiency ($\eta_{total}$) is estimated via the kinetics of the above steps together according to Equation (3):

$$\eta_{total} = \eta_{absorption} \times \eta_{separation} \times \eta_{reaction} \tag{3}$$

where $\eta_{absorption}$ is the light absorption efficiency that is the fraction of generated $e^-/h^+$ pairs excited by the incident photon flux, $\eta_{separation}$ is the charge separation efficiency that is the fraction of photogenerated charge carriers that isolate and migrate to the solid–liquid interface, and $\eta_{reaction}$ is the reaction efficiency of the gCN surface; that is, the efficiency of the surface reaction involving charge carriers at the solid–liquid interface.

Notably, the lowest band edge of the CB should be lower than the redox potential of $H^+/H_2$ (0 V vs. RHE), and the highest band edge of the VB should be greater than the chemical redox potential of $O_2/H_2O$ (Figure 3) [60,61]. Non-metal atoms provide more active sites and reaction centers on the surface of gCN, allowing delay recombination of $e^-/h^+$ [60,61]. Owing to the ultrafast rate of $e^-/h^+$ (~ps to ms), they should be promptly captured by the non-metal atoms for promoting the separation and migration of photogenerated charges along with participation in the HER.
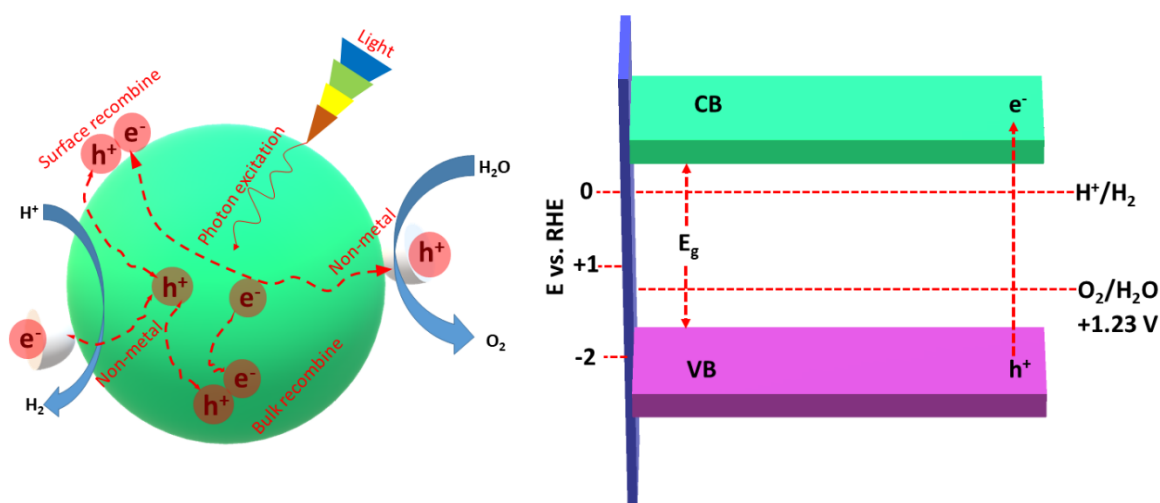


**Figure 3.** The role of non-metal dopants and the photocatalytic HER mechanism using non-metal doped porous gCN (**left**) and the band gap of gCNs relative to the required energy barrier for water splitting (**right**). This figure was designed based on the data in Ref [61].

### 3.2. Electrocatalytic HER Mechanism

Table 2 summarizes the electrocatalytic HER mechanisms in aqueous solutions of both acidic and alkaline electrolytes. In an aqueous solution of acidic electrolyte, two or three reaction pathways can take place (Equations (4)–(6)) and the HER ensues on the active site of the gCN electrocatalyst (M*):

(I)     A Volmer reaction step that includes a discharge step to allow reduction of protons on the M* and subsequent proton adsorption on M* of gCNs to form gCN-M*H$_{ads}$ (Equation (4));

(II)    A Heyrovsky reaction step that involves electrochemical desorption to desorb $H_2$ from the M* via the proton/electron transfer and regenerate of M* Equation (5);

(III)  A Tafel reaction step that includes the coupling of two adsorbed protons to release $H_2$ and the regeneration of M* (Equation (6)).

The HER mechanism in an aqueous solution of alkaline electrolyte (Equations (7)–(9)) includes Volmer–Heyrovsky or Volmer–Tafel reaction steps but with the initial dissociation of $H_2O$ on the M*, due to inferior or low proton concentration in the alkaline electrolyte.

Therefore, the additional energy needed for dissociating $H_2O$ in alkaline electrolyte is an additional energy barrier of the HER, consequently affecting the overall reaction rate and kinetics. Thus, the HER kinetics in alkaline electrolytes is extremely sluggish relative to acidic electrolytes, owing to more abundant proton donor presence (i.e., $H_3O^+$) in acidic electrolytes than (i.e., $H_2O$) in alkaline electrolytes. However, noble metals can accelerate the HER rate and kinetics in different electrolytes over broad pH ranges, while

few noble-metal-free catalysts can do this. Therefore, it remains a grand challenge to develop electrocatalysts or photocatalysts for HERs over different pH ranges (i.e., acidic, alkaline, and neutral).

**Table 2.** HER steps in an aqueous solution of acidic and alkaline electrolytes.

| Name | Equation | Equation No. |
|---|---|---|
| HER in an aqueous solution of acidic electrolyte | | |
| Volmer reaction step | $gCNs\text{-}M^* + H_3O^+ + e^- \rightarrow gCNs\text{-}M^*H_{ads} + H_2O$ | (4) |
| Heyrovsky reaction step | $gCNs\text{-}M^*H_{ads} + H_3O^+ + e^- \rightarrow gCNs\text{-}M^* + H_2 + H_2O$ | (5) |
| Tafel reaction step | $gCNs\text{-}M^*H_{ads} + gCNs\text{-}M^*H_{ads} \rightarrow 2gCNs\text{-}M^* + H_2$ | (6) |
| HER in an aqueous solution of alkaline electrolyte | | |
| Volmer reaction step | $gCNs\text{-}M^* + H_2O + e^- \rightarrow gCNs\text{-}M^*H_{ads} + OH^-$ | (7) |
| Heyrovsky reaction step | $gCNs\text{-}M^*H_{ads} + H_2O + e^- \rightarrow gCNs\text{-}M^* + H_2 + OH$ | (8) |
| Tafel reaction step | $gCNs\text{-}M^*H_{ads} + gCNs\text{-}M^*H_{ads} \rightarrow 2gCNs\text{-}M^* + H_2$ | (9) |

### 3.3. HER Measurements and Calculations

The HER process is conducted using various cyclic voltammograms (CVs), impedance spectroscopy (EIS), linear sweep voltammograms (LSVs), chronoamperometry (I-T), Tafel plots, and electrochemical impedance tests in the presence and absence of light. The potential window for a HER in a CV mainly depends on the electrolytes, including ($-0.3$ to $+1$ V in the acidic electrolyte) and ($+0.3$ to $-1$ V in the alkaline electrolyte); meanwhile, in an LSV the potential direction must be negative (0 to $-1$ V or 1.5 V)—regardless of the type of electrolyte—to allow for a reduction reaction. The I-T time ranges from a few minutes to several hours based on the catalyst's durability in the electrolyte solution; however, the long-term durability testing takes several weeks. The activity of the gCN-based photocatalysts is determined using the following calculations, summarized in Table 3.

**Table 3.** HER measurements and calculations.

| Name | Equation | Equation No. |
|---|---|---|
| Quantum efficiency (QE) | $QE\ (\%) = \dfrac{\text{number of reacted electrons}}{\text{number of incident photons}} \times 100$ | (10) |
| Current density (J) | $J = I/A$ | (11) |
| Over potential (η) | $\eta = E - E_o$ | (12) |
| Turnover frequency (TOF) | $TOF = JA/2Fm$ | (13) |
| Reduction current density vs. scan rate | $Slope = 2nFAΓ0/4RT$ | (14) |
| The turnover frequency (TOF) | $TOF = J \times NA/(F \times n \times Γ)$ | (15) |
| Energy efficiency (Eefficiency) | $Eefficiency = [Eeq/Eeq + \eta] \times EFaradic$ | (16) |
| Quantum yield | $QY = [2.nx.NA.h.c/till.I.A.\lambda]$ | (17) |
| Electrochemical active surface area (ECSA) | $ECSA = CDL/Cs$ | (18) |
| Double-layer capacitance (Cdl) | $Cdl = (\Delta j)/2dVb$ | (19) |
| Incident photon to current conversion efficiency | $IPCE\ (\%) = [(1240 \times J)/(\lambda \times Io)] \times 100$ | (20) |

The quantum efficiency (QE) is calculated using Equation (10) by dividing the number of reacted electrons by the number of the incident photons.

The current density (*J*) is calculated via the dividing of measured current (I) on the geometric surface area of the working electrode (A) Equation (11). The catalysts should be able to produce an excellent *J* value under low applied potential (V).

The overpotential ($\eta$) is calculated by Equation (12). *E* is the measured electrode's potential to deliver a current density of 10 mA/cm$^2$ or more and $E^o$ is the standard potential for water splitting ($-1.23$ V for OER and 0 V for HER). The catalysts should possess a lower $\eta$ to allow fast HER kinetics.

The turnover frequency (TOF) of each active site is calculated based on *J* and $\eta$ by Equation (13), where 2 is the number of moles of electrons consumed in the evolution of one mole of H$_2$ from H$_2$O; *F* is the Faradic constant (96,485 C/mol), and *m* is the number of active sites (mol).

The active sites (m) are extracted from the linear relationship between the reduction current densities as a function of sweeping rates, which show a linear relationship. The slope could be obtained from the graph to be used in Equation (14), where *n* is the number of electrons transferred; $\Gamma 0$ is the surface concentration of the active sites (mol/cm$^2$); *R* is the ideal gas constant and *T* is the absolute temperature.

The TOF can also be calculated using Equation (15), where NA is the Avogadro number, F is the Faraday constant, n is the number of electrons transferred (two for HER and four for OER) to generate one molecule of H$_2$ or O$_2$, and $\Gamma$ is exact number of active sites catalyzing the reaction per square meter. Therefore, catalysts with abundant active sites should provide higher TOF.

Energy efficiency ($E_{\text{efficiency}}$) is calculated by Equation (16), where $E_{\text{eq}}$ is the equilibrium potential; the energetically efficient catalyst should allow HER at a lower $\eta$ and with a high E$_{\text{Faradic}}$.

The quantum yield (QY) is calculated from Equation (17), where $n_x$ is the moles of the product; $N_A$ is Avogadro's constant ($6.022 \times 10^{23}$ mol$^{-1}$); *h* is Planck's constant ($6.626 \times 10^{-34}$ J.s); *c* is the speed of light ($3 \times 10^8$ m.s$^{-1}$); $t_{ill}$ is the light illumination time; *I* is the incident intensity (W/cm$^2$) and $\lambda$ is the wavelength of light (nm); and *A* is the irradiated area of the cell (cm$^2$).

Non-metal-doped gCNs give the CV features of rectangular shape assigned to high capacitance effect, so the electrochemical active surface area (ECSA) is calculated using the double capacitance (C$_{\text{DL}}$) via measuring the CV at different scan rates because of N$_2$-saturated aqueous electrolytes (Equation (18)), where $C_s$ is the specific capacitance of a flat surface with 1 cm$^2$ (0.015–0.110 mF/cm$^2$ in H$_2$SO$_4$), (0.022–0.130 mF/cm$^2$ in NaOH and KOH solutions) depending on the electrolyte concentration [62].

Then the double-layer capacitance (Cdl) is determined via plotting the $\Delta j$ = (ja-jc) at 0.1 V as a function of sweeping rate using Equation (19). The Cs is assumed as 20.9 $\mu$F/cm$^2$ for a flat electrode with 1 cm$^2$ of real surface area [63]. Higher ECSA is an indicator for the greater active sites.

The incident photon to current conversion efficiencies (IPCEs) are calculated using Equation (20), where $\lambda$ is the wavelength of the incident light, *J* is the photocurrent density, and $I_o$ is the incident light intensity. Thus, photocatalysts with lower bandgap energy can enhance the viable light absorption and provide higher IPCEs.

The Tafel slope is obtained from Tafel plots via plotting the $\eta$ vs. log *J*. A greater Tafel slope is an indication of quick HER kinetics and high activity.

The EIS fitting and Voigt electrical equivalent circuit are usually used for fitting the EIS data to obtain electrolyte resistance ($R_s$), charge transfer resistance ($R_{ct}$), and constant phase elements (CPE). The photocatalysts should reveal lower $R_s$ and $R_{ct}$ along with higher CPE, made evident by better electrolyte–electrode interaction and quick charge mobility.

## 4. Role of Non-Metal Dopants

Non-metal dopants can modulate bandgap energy, augment light absorption, facilitate separation of e$^-$/h$^+$ pairs, attract electrons, and enhance the separation and migration of gCN charge carriers (Figure 4). Moreover, non-metal dopants provide active sites, serve as electron sinks, generate active sites for proton reduction, and improve durability. The minimum theoretical bandgap required to drive the overall water-splitting reaction is 1.23 eV, which corresponds to a wavelength of approximately 1000 nm, so an additional

overpotential is usually needed to induce and tune the electron migration process during the HER [60,61]. The reductive decomposition potentials and CBM should be more negative than the $H^+/H_2$ potential to allow thermodynamic durability of gCN-based photocatalysts during the HER [60,61].



**Figure 4.** The molecular structures of gCNs and their merits and accommodation sites for non-metal dopants into gCNs based on data from Refs. [28,38,64].

### 4.1. Integration of Heteroatoms

The chemical structure of gCNs is still questionable; however, the most recognized structures are triazine or polyheptazine, which possess various unique properties (Figure 4). The heteroatom elements are integrated via abundant active sites. Figure 4 shows the possible substitution sites of heteroatoms (i.e., B, O, S, P, Cl, Br, I, and F) in gCNs, including the substitution of N atom with (I, S, and O), coordination of P with two N-atoms and replacement of C with B or coordination with F (C-F) (Figure 4) [60,61]. Heteroatom dopants, with their great inbuilt ionization energies and electro-negativity, can form covalent bonds by gaining electrons when reacting with other compounds. Meanwhile, the physicochemical properties (i.e., size, electronegativity, and chemical state) and location of non-metal dopants can tune the catalytic and photocatalytic properties of gCN.

### 4.2. Non-Metal-Doping Configuration and Effects

Unlike noble metals (i.e., Pt, Pd, Au, and Ru) and transition metals (i.e., Co, Cu, and Ni), non-metal dopants are earth-abundant and inexpensive, enhancing electrical conductivity, hydrophilicity, and active sites [60,61,65]. This is due to electron-donating or electron-withdrawing characteristics that tailor the electronic, catalytic, and photocatalytic properties of gCNs. Non-metal atoms can act as trapping sites facilitating the generation of electron–hole pairs, delaying their recombination, and enhancing light absorption under

light illumination [60,61]. Table 4 summarizes the main advantages and disadvantageous of heteroatom-doped porous gCN.

**Table 4.** Comparison of the advantages and disadvantages of mono-heteroatom-doped porous gCNs.

| Doping | Advantages | Disadvantages |
|---|---|---|
| N | Generates abundant defects and active sites<br>Increases electronic conductivity<br>Promotes ion adsorption<br>Earth-abundant and inexpensive<br>Modulates the Fermi level, bandgap, and localized electronic state<br>Eases the generation of electron–hole pairs and delays their recombination<br>Enhances light absorption | Not durable at elevated temperatures<br>Does not enlarge interlay distance<br>Uncontrolled doping sites and concentration<br>Cumbersome process<br>High operating temperature |
| S | Expands interlayer distance<br>Induces reduction reaction<br>Promotes ion adsorption/diffusion<br>Modulates the Fermi level, bandgap, and localized electronic state<br>Facilitates the generation of electron–hole pairs and delays their recombination<br>Enhances light absorption | Leads to structural deformation<br>Uncontrolled doping sites and concentration<br>High operating temperature<br>Slow preparation process |
| P | Enlarges interlayer distance<br>Enhances ion adsorption/diffusion<br>Upsurges geometric distortion<br>Alters the Fermi level, bandgap, and localized electronic state<br>Induces creation of electron–hole pairs and prevents their quick recombination<br>Enhances light absorption | Causes large structural distortion<br>Uncontrolled doping sites and concentration<br>High operating temperature<br>Slow preparation process |
| B | Generates massive in-plane defect<br>Enhances ion adsorption/diffusion<br>Modulates the Fermi level, bandgap, localized electronic state, and spin density<br>Induces creation of electron–hole pairs and prevents their quick recombination<br>Enhances light absorption | Difficult to prepare<br>Forms high-energy trap<br>Uncontrolled doping sites and concentration |
| F | Enlarges interlayer distance<br>Enhances ion adsorption/diffusion<br>Enhances electronic conductivity<br>Suppresses the John–Teller effect<br>Modulates the Fermi level, bandgap, and localized electronic state | Causes large structural deformation upon cycling<br>Excess doping causes rapid capacity disappearance<br>Hazardous precursors<br>Uncontrolled doping sites and concentration |

A N atom, with its size (~155 pm) being close to a carbon atom (~170 pm) but with a larger electronegativity (~3.04) than carbon (2.55) can withdraw electrons, generate abundant active sites, and boost the electronic and ionic conductivity of carbon [6,38,60,61]. Meanwhile, the N atom creates electron-deficiency on its adjacent positive C atom with its negative charge, allowing for a dipole $N^-$-$C^+$ bond, which makes gCN more feasible for electrophilic and nucleophilic attack in addition to accelerating charge mobility and facilitating the dissociation of $H_2O$ molecules during a HER [64,66–70]. N-doping into gCN can result in N atom pyridinic, pyrrolic/pyridonic, quaternary/graphitic, and pyridine-N-oxide that show binding energy at 398.5, 400.1, 401.1, and 403.2 eV, respectively, as determined by X-ray photoelectron spectroscopy (XPS) [71]. These N atom species are highly active sites for $CO_2RR$ and other catalytic applications, which induce Lewis basicity on the C atom and act as active sites during HERs.

The boron (B) atom, with a smaller size of (85 pm) and lower electronegativity (2.04) than C, is inserted into the skeleton structure, as it replaces C in the gCN without affecting its planar structure [35,38–40]. B, with its electron-deficiency that accounts for boron being a strong Lewis acid that can easily accept protons, decreases the Fermi level into valance, and promotes charge polarization of gCNs. Moreover, B can decrease the Fermi level into valance, generate multiple defects, enhance visible light absorption, modulate bandgap energy, and enhance the reactivity of gCN [35,38–40]. According to the XPS, there are two main in-plane binding structures of B in gCN, including graphitic B at 200.5 eV and B-substituted C atoms in the hexagonal triazine or polyheptazine rings of co-conjugated gCN at 198.5 eV [72]. Interestingly, B can stabilize the negatively polarized oxygenated atoms during the HER, consequently enhancing $H_2O$ molecule chemisorption from the electrolyte during the HER process.

Sulfur (S), with a larger size (180 pm) and higher electronegativity (2.58) than carbon, promotes the electrical conductivity and spin density, edge strain, and charge delocalization of gCN via the substitution of the N atom with S in gCN [35,38–40]. Thus, the C-S bond in triazine or polyheptazine at the edges of gCN is easily determined by the XPS at a binding energy of 163.7 eV.

Phosphorus (P), with lower electronegativity (2.19) and large size (195 pm) than C, creates positive charges on P dopant and negative charges on positively charged C. This leads to the formation of ($P^+$-$C^-$) via the co-coordination of P with two C atoms in triazine or polyheptazine of gCN, which can promote charge mobility and provide plentiful active sites during a HER [35,38–40]. A C-P bond is detected at a binding energy of 132.5 eV.

The oxygen (O) atom has a lower atom size (152 pm) than C but a higher electronegativity (3.44 pm), which increases the positive charge on its neighboring C atom in the form of ($C^+$-$O^-$) after substitution of N with O in gCNs [35,38–40]. This allows more electron donation to generate additional active sites, boosting the electronic and ionic conductivity of gCN. Additionally, the O atom alters the intrinsic electronic structure of gCN, which is important for controlling the binding energies of reactants and intermediates during HER, due to oxidant functional groups (i.e., C-O, C=O, and C-OH), which can induce in situ formation of active oxygen species (i.e., -OH, $O_2$) needed for activation and dissociation of $H_2O_2$. The XPS can detect C-O bonds at 532 eV and C=O 533 eV. However, the exact location of heteroatoms in the skeleton structure of gCNs and their effect is still ambiguous. Additional theoretical and experimental studies are needed, along with in situ characterization tools, to determine their position and effects during catalytic and photocatalytic reactions.

## 5. Heteroatom-Doped Porous Carbon Nitride

Nowadays, various types of carbon nitride nanostructures, including nanosheets, nanotubes, and nanoflowers, have been designed as highly efficient photocatalysts for HERs [65,73–76]. Heteroatom-doped porous carbon nitride, which combines the advantages of both heteroatom dopants and the porous structure of carbon nitride, can further extend light adsorption, increase active sites, and facilitate charge transfer and separation, thus enhancing photocatalytic performance [60,77–79]. There are various approaches to doping of gCNs with various heteroatoms. Table 5 shows the advantages and disadvantages of the main methods for the preparation of doped gCNs.

**Table 5.** Comparison between the preparation methods of doped gCN nanostructures based on data from Refs. [60,80–88].

| Methods | Precursors | Doping | Advantages and Disadvantages |
|---|---|---|---|
| Thermal annealing | Boric trioxide<br>Boron trichloride<br>Boron trioxide<br>Ammonia<br>Diammonium hydrogen<br>Urea<br>Hydrogen sulfide<br>Diaminodiphenyl sulfone<br>Dibenzyl sulfide<br>Sulfur powder<br>Hexachlorocyclotriphosphazene<br>Phosphoric acid<br>Diammonium phosphate<br>Hexafluorophosphate<br>Ammonium fluoride<br>Ammonium chloride<br>Ammonium bromide | B<br>B<br>B<br>N<br>N<br>N<br>S<br>S<br>S<br>S<br>P<br>P<br>P<br>P<br>F<br>Cl<br>Br | Simple, one-pot, feasible for various precursors (i.e., gases, liquids, and solids), tunable doping.<br>Limitations: high operation temperature and energy consumption |
| Physical vapor deposition (PVD) or chemical vapor deposition (CVD) | Boric acid<br>Phenylboronic acid<br>Ammonia<br>Iodine<br>Pyrimidine | B<br>B<br>N<br>I<br>N | Allows simultaneous growth of doped gCNs with controllable doping<br>Limitations: complex process, energy consumption, requires special laboratory equipment, and generates waste gases<br>Limitations: high cost, inferior yield, and feasible for low ranges of precursors |
| Ball milling | Ammonia<br>sulfur powder<br>Ammonium fluoride<br>Ammonium chloride<br>Ammonium bromide | N<br>S<br>F<br>Cl<br>Br | Low-cost, facile, and scalable process<br>Limitations: doping only at edges<br>Limitations: uncontrolled doping process |
| Bottom-up synthesis | Boron tribromide<br>Lithium nitride<br>Pentachloropyridine<br>Thiourea | B<br>N<br>N<br>S | Highly productive, solution-based, need mild conditions<br>Limitations: inevitable high oxygen content and uncontrollable doping |
| Wet chemical method | Hydrazine<br>Ammonium thiocyanate<br>Hydrogen fluoride<br>Hydrogen iodide<br>Ammonium chloride<br>Ammonium bromide<br>Boric acid | N<br>S&N<br>F<br>I<br>Cl<br>Br<br>B | Inexpensive, low energy consumption, solution-based, productive, easy process, and feasible for wide ranges of precursors<br>Limitations: low-doping content and uncontrollable doping |
| Plasma | $N_2$<br>$Cl_2$<br>Hydrogen sulfide | N<br>Cl<br>D | Quick process and inferior power consumption<br>Limitations: low yield and feasible for specific precursors |
| Arc-discharge | $NH_3$<br>Pyrrole<br>Boron trioxide | N<br>N<br>B | Productive and quick process<br>Limitation: high energy consumption (i.e., voltage and current)<br>Limitation: inferior and uncontrollable doping content |

### 5.1. Mono Heteroatom Doped Porous Carbon Nitride

Table 6 summarizes diverse mono-heteroatoms including phosphorus [76,89–103], sulfur [104–114], boron [115–121], oxygen [122–134], carbon [135–139], nitrogen [140–142], and halogens [143–146] doped porous carbon nitride catalysts, and their photocatalytic hydrogen production performance. Moreover, the effect of morphology, preparation methods, and light source on the $H_2$ production rate and stability on mono-heteroatom-doped porous gCNs is also summarized in Table 6.

**Table 6.** Comparison of photocatalytic performance of mono heteroatom doped porous carbon nitride toward HER.

| Photocatalysts | Doping Element | Morphology | Synthetic Method | Co-Catalyst | Light Source | H$_2$ Evolution Rate ($\mu$mol h$^{-1}$g$^{-1}$) | Apparent Quantum Efficiency | Durability | Ref |
|---|---|---|---|---|---|---|---|---|---|
| P-CN | P | Mesoporous nanostructured flowers | Template-free co-condensation method | 3 wt% Pt | 300 W Xeon arc lamp | 2082 | | No obvious attenuation of H$_2$ evolution rate after illumination of 16 h | [76] |
| PCN-S | P | Porous nanosheets | Thermal polycondensation of melamine-2-aminoethylphosphonic acid complex, followed by thermal exfoliation | 1 wt% Pt | 300 W Xe arc lamp with a UV-cutoff filter (>400 nm) | 1596 | 3.56% at 420 nm | | [89] |
| P10-550 | P | Layered platelet-like morphology | Thermally induced copolymerization route using hexachlorocyclotriphosphazene as P source and guanidinium hydrochloride as g-C$_3$N$_4$ precursor. (10 wt%P, calcination temperature = 550 °C) | 3 wt% Pt | 300 W xenon lamp with a 420 nm cutoff filter | 506 | | The hydrogen amount is still comparable to that of first cycle after five cycles | [90] |
| P-TCN | P | Hexagonal tubes with micro-nanostructure | Pyrolysis of the melamine–cyanuric acid supramolecular precursor formed by phosphorous acid-assisted hydrothermal method | 1 wt% Pt | 300 W Xeon arc lamp with bandpass filter (365, 420, 450, 520, and 600 nm) | 670 | 5.68% at 420 nm | No noticeable deterioration after irradiation for 20 h | [91] |
| CN-SP | P | Tubular g-C$_3$N$_4$ with surface carbon defects | Thermal polymerization of a supramolecular precursor formed under pyrophosphate–assisted hydrothermal process | 1 wt% Pt | 300 W Xe arc lamp with a $\geq$420 nm cutoff filter | 570 | | | [92] |
| P-CNRs | P | Macro/mesoporous g-C$_3$N$_4$ micro-rods | Direct calcination of reflux-treated ethylene diphosphonic acid–melamine complex fiber network | 3 wt% Pt | 300 W Xe arc lamp with a $\geq$420 nm cutoff filter | 4960 | | No obvious decay after irradiation for 20 h | [93] |
| P0.01 | P, Na | Porous multi-layer nanosheets | Polymerization of the mixed precursors of melamine and sodium tripolyphosphate | 1 wt% Pt | 350 W Xe arc lamp | 3820 | | No decrease in H$_2$ production rate after irradiation for 12 h | [94] |
| PCNNFs | P | Fragmented nanoflakes | First P-doping via using phytic acid biomass as P source and urea as C$_3$N$_4$ precursor, followed by posttreatment | 3 wt% Pt | 300 W Xe arc lamp with a >420 nm cutoff filter | 15,921 | 6.74% at 420 nm; 0.24% at 600 nm | No obvious decay in photocatalytic H$_2$ production under irradiation for 50 h | [95] |
| PCNT | P | Hierarchical coral-like porous tubes | Pyrolysis and freeze-drying using dicyandiamide as carbon nitride source and phytic acid as P source | 3 wt% Pt | 300 W Xe arc lamp with a $\geq$420 nm cutoff filter | 2020 | 4.32% at 420 nm; 3.58% at 450 nm; 1.28% at 500 nm | H$_2$ production rate kept almost same after 10 h reaction | [96] |
| PCN1.5 | P | Flower-like structure consisting of multitudinous nanosheets | Template-free and thermal copolymerization route using phosphoric acid as P source and cyanuric acid–melamine complex as supramolecular precursor | 3 wt% Pt | 300 W Xe lamp with a 400 nm UV-light cutoff filter | 5128 | | Only about 7.3% attenuation was observed after visible light illumination of 16 h | [97] |
| PCN-50 | P | Platelet-like surface | Polymerization of urea and NH$_4$H$_2$PO$_2$ at 570 °C for 3 h | 1 wt% Pt | 300 W Xe lamp with a 400 nm UV-light cutoff filter | ~9167 | | Photocatalytic performance was maintained through 20 h of cycling experiments | [98] |
| PCN(1.6) | P | Nearly transparent nanosheets agglomerate | The calcination of polymeric carbon nitride formed by urea condensation and amorphous phosphorus | 3 wt% Pt | 300 W Xe arc lamp as simulated sunlight (>300 nm) or with a 420 nm cutoff filter | 8707 and 5720 under the simulated solar light and visible light | | | [99] |

**Table 6.** *Cont.*

| Photocatalysts | Doping Element | Morphology | Synthetic Method | Co-Catalyst | Light Source | H$_2$ Evolution Rate ($\mu$mol h$^{-1}$g$^{-1}$) | Apparent Quantum Efficiency | Durability | Ref |
|---|---|---|---|---|---|---|---|---|---|
| P-CNTS | P | Tubular structure with a large number of pores in the walls | Pre-hydrothermal and calcination under a nitrogen atmosphere | 1 wt% Pt | 300 W Xe lamp with a 420 nm UV-light cutoff filter | 2749.3 | | The amount of produced hydrogen slightly decreased after three cycles of tests | [100] |
| L-PCN-1.0 | P | Louver-like nanowire arrays | Supramolecular self-assembly of melamine–cyanuric acid | 1 wt% Pt | 300 W Xe arc lamp with a ≥420 nm cutoff filter | 1872.9 | 6.93% at 420 ± 15 nm | The hydrogen production has no noticeable deactivation over four cycles | [101] |
| PCN-HMS | P | Hierarchical mesoporous microspheres | Supramolecular chemistry-mediated one-pot strategy | 1 wt% Pt | 300 W Xe lamp with an ultraviolet cut-off filter ($\lambda \geq$ 420 nm) | 1820 | | | [102] |
| PO-CN | P | Porous ultrathin nanosheets | Two-step thermal treatment | 3 wt% Pt | 300 W Xe lamp with a 420 nm cutoff filter | 997.7 | | | [103] |
| NiSCN | S, Ni | Nanosheets | High-temperature thermal polymerization of urea and benzyl disulfide | 5 wt% Ni | 300 W Xe arc lamp with a cutoff filter ($\lambda >$ 420 nm) | 2021.3 | 2.51% at 420 nm | The H$_2$ production rate decreases a little after four cycles for 20 h | [104] |
| MTCN-6 | S | Rectangular rods | Self-assembly of melamine with tri-thiocyanuric acid, followed by calcination | 1 wt% Pt | 300 W Xe arc lamp with a cutoff filter ($\lambda >$ 420 nm) | 1511.2 | 3.9% at 420 nm | No obvious decrease in H$_2$ generation rate over five cycles | [105] |
| PCNS-2 | S | Ultrathin nanosheets with porous networks | The polymerization of thiourea and NH$_4$Cl at 550 °C for 3 h | | 300 W Xe arc lamp with a cutoff filter ($\lambda >$ 420 nm) | ~367 | | No obvious decrease of H$_2$ evolution rate within four cycles | [106] |
| CN-0.20%Dx-25 | S,K | Needle-like nanorods | Condensation of thiourea and dithiooxamide followed by post-treatment in molten salt | Pt | 300 W Xe arc lamp with a cutoff filter ($\lambda >$ 420 nm) | 1962.10 | | Obvious decrease in the photocatalytic H$_2$ evolution performance due to K leaching | [107] |
| 2D-SCN | S | Nanosheets | Polycondensation of thiourea, followed by thermal oxidative treatment | 1 wt% Pt | 140 W Xe lamp | 8493 | 8.35% at 420 nm | The hydrogen evolution activity was maintained after 36 h of continuous irradiation | [108] |
| S/g-C$_{3+x}$N$_{4+y}$ | S, cyano group | Porous leaf with irregular shape | Treating pristine g-C$_3$N$_4$ nanosheets under acetonitrile and hydrogen sulfide atmosphere | 3 wt% Pt | 300 W Xe lamp with a UV light filter ($\lambda >$ 420 nm) | 1901 | 33.5% and 13.1% at 405 and 420 nm | The amount of produced hydrogen was decreased in first three cycles, but returned to the previous high level after the re-addition of TEOA sacrificial agent | [109] |
| S-CN(0.1) | S | Holey nanosheets | One-step thermolysis of thiocyanuric acid | 3 wt% Pt | 300 W Xe lamp with a UV light filter ($\lambda >$ 420 nm) | 6225.4 | 10% at 420 ± 10 nm | The photocatalytic HER stabilizes at ca. 6200 $\mu$mol h$^{-1}$g$^{-1}$ under five cycles of reuse | [110] |

**Table 6.** *Cont.*

| Photocatalysts | Doping Element | Morphology | Synthetic Method | Co-Catalyst | Light Source | H$_2$ Evolution Rate (μmol h$^{-1}$g$^{-1}$) | Apparent Quantum Efficiency | Durability | Ref |
|---|---|---|---|---|---|---|---|---|---|
| PCNS | S | Layered structure | One-step auxiliary thermal polycondensation of melamine and ammonium persulfate | 2 wt% Pt | 300 W Xenon lamp with a 420 nm UV-cutoff | 58,680 | | No obvious decrease of H$_2$ production after three cycles | [111] |
| SCN1.0 | S | Peony-like morphology | Thermal condensation of cyanuric acid–melamine–trithiocyanuric acid complex under N$_2$ atmosphere | 3 wt% Pt | 300 W Xe lamp | 11,354 | 13.69% at 420 nm | Only about 3.2% attenuation of photocatalytic hydrogen production after four cycles | [112] |
| mpgCNS | S | Mesoporous nanosheet | Pyrolysis of thiourea using SiO$_2$ nanoparticles as the hard template | 3 wt% Pt | 300 W Xe lamp with a 420 nm cutoff filter | 1360 | 5.3% at 420 nm | 10% activity drop over the photoreaction for 72 h with evacuation at every 12 h | [113] |
| CN-MT | S | Nanoporous microrods | Thermal condensation of melamine-trithiocyanuric acid supramolecular cocrystal under N$_2$ atmosphere | 1 wt% Pt | 500 W Xe lamp with a 400 nm filter | 5000 | | No loss of catalytic activity after the catalytic H$_2$ evolution for 60 h | [114] |
| SCN-HMS | S | Mesoporous microspheres | Supramolecular chemistry-mediated one-pot strategy | 1 wt% Pt | 300W Xe lamp with an ultraviolet cutoff filter (λ ≥ 420 nm) | 2230 | 3.8% at 420 nm | No obvious decrease was observed for the H$_2$ evolution rate even after four cycles | [102] |
| B-SSCN | B | Microsphere | One-step solvothermal method by using cyanuric chloride and cyanuric acid as precursors and ammonia borane as B source | 3 wt% Pt | 300 W Xenon lamp with a UV cutoff filter (λ > 420 nm) | 910 | ~1.15% at 420 nm | The H$_2$ evolution rate was well preserved after four test cycles over 4 days and no structure change after reaction | [115] |
| CNB NS | B | Porous ultrathin nanosheet | Reforming and thermal condensation of barbituric acid and melamine | 3 wt% Pt | 300 W Xe lamp with a UV cutoff filter (λ > 400 nm) | 1323.25 | 7.45% at 420 nm | The amount of H$_2$ production increase steadily with extended the reaction time and no significant deactivation is observed after five cycles | [116] |
| B-CNNT | B | Ordered nanotubes | Hydrothermal and calcination of melamine and boric acid | Pt | 300 W Xenon lamp with a UV cutoff filter (λ > 420 nm) | 22,100 | 7.33% at 420 nm | The H$_2$ production increases steadily with time and retain stability | [117] |
| B, CsCN-Ns | B, Cs | Porous and wrinkled nanosheets | Recrystallization of melamine in water in the presence of boric acid and CsCl followed by calcination and thermal etching | 3 wt% Pt | Xenon lamp with a cutoff filter (λ ≥ 420 nm) and IR filter | 1120 | | The H$_2$ production rate was stable in five successive cycles | [118] |
| B/g-C$_3$N$_4$ | B | Nanosheets | The pyrolysis of urea and 1-ethyl-3-methylimidazolium tetrafluoroborate | 0 | 350 W Xenon lamp with a UV cutoff filter (λ > 365 nm) | 901 | | The photocatalytic activity remains unchanged after three reaction cycles | [119] |

**Table 6.** *Cont.*

| Photocatalysts | Doping Element | Morphology | Synthetic Method | Co-Catalyst | Light Source | H$_2$ Evolution Rate ($\mu$mol h$^{-1}$g$^{-1}$) | Apparent Quantum Efficiency | Durability | Ref |
|---|---|---|---|---|---|---|---|---|---|
| PNCN-BNa-3 | B, Na | Porous nanosheets | Controlling the heating rate and thermal posttreatment using melamine nitrate as precursor, sodium borohydride as B source and Na source | 1.2 wt% Pt | 10 W white LED lamp ($\lambda$ > 420 nm) with the color temperature of 6500 K | 5971.51 | 9.39% at 430 nm | Even after five cycles of photocatalytic test, the hydrogen generation activity is not significantly reduced | [120] |
| D-TCN$_{450}$ | B | Hollow tube | Self-supramolecular reaction and NaBH$_4$ thermal reduction approach | 3 wt% Pt | 300 W Xe lamp with a 420 nm cutoff filter | 789.2 | | | [121] |
| O-doped g-C$_3$N$_4$ | O | Irregular porous structure with hierarchical edges | Hydrothermal treatment of g-C$_3$N$_4$ with H$_2$O$_2$ at 140 °C for 10 h | 1.2 wt% Pt | 300W Xe arc lamp with a UV-cutoff filter ($\lambda$ < 420 nm) | 375 | | The H$_2$ evolution remains stable in the recycling three runs | [122] |
| MCN | O | Porous network composed by nanosheets | Condensation of supramolecular aggregates formed by H$_2$O$_2$-treated melamine | 3 wt% Pt | 300 W Xenon lamp with a 420 nm filter | 1204 | 7.8% at 420 nm | A stable HER rate within 25 h | [123] |
| HS-g-C$_3$N$_4$-O | O | Holey thin sheets | Using photo-Fenton reaction in the presence of Fe$^{3+}$/Fe$^{2+}$ and H$_2$O$_2$ | 5 wt% Pt | 300W Xe lamp with 420 nm filter | 6752 | | The H$_2$ evolution rate is quite stable under continuous irradiation of 26 h | [124] |
| P-CNO | O | Porous nanosheet with highly ordered architecture | Heating the hydrothermally treated dicyandiamide at 550 °C for 2 h | 1 wt% Pt | 300 W Xeon lamp with a UV cutoff filter ($\lambda$ > 400 nm) | 1748.6 | 7.2% at 420 nm | The hydrogen production performance shows no trend of deactivation even after 15 h | [125] |
| GCN-4 | O | Three-dimensional porous nanosheets | Water-based homogeneous supramolecular assembly | 3 wt% Pt | 300 W Xeon-lamp equipped with a 420 nm-cutoff filter | 1968 | 10.3% at 420 nm | A stable HER rate after six cycling trips | [126] |
| p-CN2 | O | Loose and porous layers | A simple co-pyrolysis of dicyandiamide and ammonium persulphate | 3 wt% Pt | 300 W Xeon lamp with a UV cutoff filter ($\lambda$ > 420 nm) | 395.96 | 0.79% at 420 nm | The photocatalytic H$_2$ production activity is well retained after four successive cycles while the phase structures are not changed | [127] |
| POCN | O | Nanosheet | Thermal polymerization reaction of melamine and ethanol | 1 wt% Pt | 300 W Xe lamp equipped with a 420 nm cutoff filter | 1286 | 12.06% at 420 nm | The HER is no apparent attenuation after four cycles | [128] |
| CN3 | O | Numerous macropores and mesopores with an assembling flake | Pyrolyzing H$_2$SO$_4$ and HNO$_3$ modified melamine precursors | 3 wt% Pt | 300 W Xe arc lamp with an AM 1.5 optical filter | 3700 | 20.88% at 420 nm | No significant decline of H$_2$ production is observed after five runs within 5 h | [129] |
| W,O/g-C$_3$N$_4$ | W/O | Hollow tubular structure | One-step polycondensation of ammonium metatungstate hydrate and melamine | 1 wt% Pt | 300 W Xe lamp with a cutoff filter ($\lambda$ > 400 nm) | 403.57 | | | [130] |

**Table 6.** *Cont.*

| Photocatalysts | Doping Element | Morphology | Synthetic Method | Co-Catalyst | Light Source | H$_2$ Evolution Rate ($\mu$mol h$^{-1}$g$^{-1}$) | Apparent Quantum Efficiency | Durability | Ref |
|---|---|---|---|---|---|---|---|---|---|
| U/AC$_{0.5}$ | O | Loose and rich bread-like porous structure | Thermal polymerization of urea and foaming agent azodicarbonamide | 3 wt% Pt | 300 W Xe lamp equipped with a 420 nm cutoff filter | 4470 | 13.0% at 400 nm | No significant decrease in photocatalytic performance after five cycles | [131] |
| OCN-3 | O | Hollow and monolayered nanosheet | Multiple thermal treatments under the N$_2$/O$_2$ atmosphere | 3 wt% Pt | 300 W Xenon lamp with an optical filter ($\lambda$ > 420 nm) | 3519.6 | 26.96% at 400 nm | Only 10.4% activity loss after 20 h | [132] |
| FCN15 | O | Rod | Calcinating supramolecular precursors prepared from acid (or alkali) and melamine | 3 wt% Pt | 300 W Xenon lamp | 12,766 | 9.4% at 420 nm | The FT-IR and Raman spectra did not change significantly after 16 h cycle test | [133] |
| OCNT | O | Ultralong hollow chain-ball | Facile supramolecular self-assembly route | 2 wt% Pt | 300 W Xe lamp equipped with a 420 and 510 nm cutoff filter | 5470 | 9.4% at 420 nm and 2.1% at 510 nm | The hydrogen production rate did not attenuate after six consecutive photocatalytic reactions | [134] |
| m-CN-0.067 | C | Nanosheet | Copolymerizing barbituric acid with melamine via microwave-assisted heating | 0.5 wt% Pt | 300 W Xe lamp equipped with a 420 nm cutoff filter | 2500 | | They offer slightly reduced H$_2$ generation during the course of 15 h visible light irradiation | [135] |
| C-rich g-C$_3$N$_4$ | C | Nanosheet | A hydrothermal–conjugate–copolymerization strategy | 0 | 300 W Xe lamp equipped with a 420 nm cutoff filter | 125.1 | 6.8% at 420 nm | No noticeable deterioration of stability activity is observed after three cycles test | [136] |
| CDCN-20 | C | Thinner nanosheet enriched with many small holes | Co-polymerization of dicyandiamide with acrylamide | 3 wt% Pt | 300 W Xe lamp with a 420 nm filter | 1266.8 | 10.14% at 420 nm | No apparent decrease in photocatalytic activity is observed after four cycling test | [137] |
| Nic-CN | C | 1D thin, porous strip-like structure | Calcination of strip-like supramolecular precursor formed by organic molecular self-assembly of melamine and nicotinic acid | 1 wt% Pt | 300 W Xe lamp ($\lambda$ > 420 nm) | 6310 | 6.8% at 420 nm | No obvious attenuation in hydrogen evolution after 5 times of cycling | [138] |
| CN-40 | C | Hollow tubular structure | Hydrothermal calcination method using melamine and sodium alginate as precursors | 3 wt% Pt | 300 W Xe lamp with a 420 or 400 nm cutoff filter | 1210.3 | 3.16% at 420 nm | More than 56% of original performance can be remained after four runs of reaction | [139] |
| C$_3$N$_{4+X}$ | N | Nanosheet | Co-thermal condensation of precursor with nitrogen-rich additive | 3 wt% Pt | 300 W Xeon lamp with a 400 nm cutoff filter | 553.5 | | The amount of produced hydrogen increased linearly with the consecutive irradiation time | [140] |
| CNNTs | N | Hollow nanotube | Supermolecule self-assembly method | 3 wt% Pt | 300 W Xe lamp ($\lambda$ > 420 nm) | 18,060 | 12.55% at 420 nm | The photocatalytic hydrogen evolution kept stable over four cycles | [141] |

**Table 6.** *Cont.*

| Photocatalysts | Doping Element | Morphology | Synthetic Method | Co-Catalyst | Light Source | H₂ Evolution Rate ($\mu$mol h$^{-1}$g$^{-1}$) | Apparent Quantum Efficiency | Durability | Ref |
|---|---|---|---|---|---|---|---|---|---|
| CNU-DMF | N | Porous nanosheets | One-step thermal copolymerization of urea and N,N-dimethylformamide | 3 wt% Pt | 300 W Xe lamp ($\lambda$ > 400 nm) | 5268 | 11.4% at 420 nm | No obvious decrease after four cycles of reaction within 16 h | [142] |
| Cl-pdg-CN-M-3 | Cl | Accumulation of thin sheets | Pyrolysis of the mixture of melamine and NH₄Cl | 3 wt% Pt | 300 W Xe lamp with a 400 nm cutoff filter | 833 | | The H₂ produced increased steadily with irradiation time lengthened in each run without noticeable deactivation | [143] |
| Cl-p-C₃N₄ | Cl | Ultrathin nanostrips | Calcination of melamine and tetrachloroterephthalonitrile in an inert atmosphere | 1 wt% Pt | 300 W Xenon lamp with a 420 nm cutoff filter | 5976 | 8.91% at 420 nm | The H₂ production rate has no apparent inactivation after four cycles | [144] |
| CNI | I | Loose and porous structure | Calcination of self-assembly precursors prepared from urea and ammonium iodide | 1 wt% Pt | 300 W Xe lamp equipped with a 420 nm cutoff filter | 3800 | 3.3% at 420 nm | Excellent cycle stability in photocatalytic hydrogen production | [145] |
| CNU-Br₀.₁ | Br | Layered platelet-like and curl-like thin nanosheet | A facile co-condensation strategy by using urea and ammonia bromine as starting materials | 3 wt% Pt | 300 W Xe-lamp equipped with an appropriate long pass cutoff filter | 240 | | No activity decrease was seen after four consecutive cycles' reaction | [146] |

### 5.1.1. Phosphorus Doping

Qiao's group reported the synthesis of porous P-doped $g$-$C_3N_4$ nanosheets (PCN-S) by using melamine (ME) and 2-aminomethyl phosphonic acid (AEP) as $g$-$C_3N_4$ precursor and P source, respectively [89]. As shown in Figure 5a, ME and AEP are first tightly coupled via acid–base interaction and van Der Waals' force to form a ME-AEP complex. After evaporation and thermal polycondensation, bulk P-doped $g$-$C_3N_4$ (PCN-B) are synthesized. PCN-S were obtained by thermal exfoliation of PCN-B; thus, numerous macropores generated by AEP decomposition can be exposed. As a reference, bulk P-doped $g$-$C_3N_4$*(PCN-B*) was prepared by using $(NH_4)_2HPO_4$ as a P source. Bulk $g$-$C_3N_4$ (CN-B) was prepared under identical conditions to that of PCN-B except for the addition of AEP. $g$-$C_3N_4$ nanosheets (CN-S) were prepared by thermal exfoliation of CN-B under identical conditions to that of PCN-S. Based on XPS and calculation results, all the doped P atoms replace the more energy-favorable C site to form a P-N bond in PCN-S. Moreover, unlike the conventional band gap narrowing, they found that P doping can induce the appearance of an empty midgap state in PCN-B and PCN-S (Figure 5b), thus extending the visible light-harvesting ability of the photocatalytic HER. As confirmed by steady-state and time-resolved photoluminescence spectroscopy and electrochemical impedance spectra measurements, PCN-S exhibits the highest separation and transfer efficiency of photo-excited electron–hole pairs. Among these photocatalysts, PCN-S possesses excellent $H_2$ production activity of 1596 $\mu$mol h$^{-1}$g$^{-1}$, which is 14.8, 10.4, 3.7, and 3.1 times higher than that of CN-B (108 $\mu$mol h$^{-1}$g$^{-1}$), PCN-B* (153 $\mu$mol h$^{-1}$g$^{-1}$), CN-S (437 $\mu$mol h$^{-1}$g$^{-1}$), and PCN-B (510 $\mu$mol h$^{-1}$g$^{-1}$), respectively (Figure 5c). Thus, the $H_2$ production activity of PCN-S (1596 $\mu$mol h$^{-1}$ g$^{-1}$) and apparent quantum efficiency (3.56%) are among the highest-reported metal-free free $g$-$C_3N_4$ photocatalysts. This is due to the porous morphology and high surface area of PCN-S (122.6 m$^2$/g) that was 1.4, 14.7, and 21.8 times of CN-S (84.2 m$^2$/g), PCN-B (8.3 m$^2$/g), and CN-B (5.6 m$^2$/g), respectively. Therefore, not only does a porous nanostructure enhance the surface area, provide more active sites, and ease diffusion of reactants and products during the HER, but it also promotes light harvesting and accelerates the transfer of photogenerated charge carriers from inner to the outer active sites results in enhancement photocatalytic HER activity. CN-B showed inferior HER activity due to its non-porous and solid agglomerate shape. This study indicated the significant effect of porous structure and P doping on enhancement the HER activity. In another study, Fang et al. realized the broader and stronger sub-bandgap adsorption by fabricating P-doped $g$-$C_3N_4$ nanoflakes (PCNNFs) using phytic acid and urea as P source and $g$-$C_3N_4$ precursor, respectively [95]. The ultrathin nanoflakes assembled in a porous network-like shaped enlarged surface area, with broad light adsorption of up to 800 nm, a reduced charge-to-surface migration path in in-vertical-plane and in-plane directions, and improved charge separation and transfer efficiency, which synergistically promoted the outstanding photocatalytic $H_2$ production rate of 15,921 $\mu$mol h$^{-1}$g$^{-1}$ and a quantum efficiency of 6.74% at 420 nm.

Thus, engineering the morphology of gCN nanostructures can benefit the separation and movement of photogenerated charge pairs, facilitate mass transfer, and offer more accessible active sites for catalytic reactions [6,28,100,101]. For instance, Zhu et al. proposed a template-free synthesis of mesoporous phosphorus-doped $g$-$C_3N_4$ nanoflowers (P-CN) with in-plane mesopores (3–18 nm) and open-up surface (Figure 5d) by co-condensation and thermolysis of a mixture with ME as $g$-$C_3N_4$ precursor and (hydroxyethylidene) diphosphonic acid as phosphonic source [76]. EDS mapping showed the presence of C, N, and P in P-CN; meanwhile, the XPS analysis demonstrated that P mainly replace C or N in $g$-$C_3N_4$ framework to form P-N or P-C bonds. Compared with pristine $g$-$C_3N_4$, mesoporous $g$-$C_3N_4$ and $g$-$C_3N_4$ nanosheets, the combination of novel morphology and P doping endows P-CN with excellent $H_2$ evolution activity. This is seen in the higher $H_2$ evolution rate of P-CN (104.1 $\mu$mol h$^{-1}$) that is 9.29 times more than the bare $g$-$C_3N_4$ reference (11.2 $\mu$mol h$^{-1}$), implying the effects of a porous flower-like shape and P-doping, which enhance the mobility of the charge carriers and HER photocurrent as further shown in (Figure 5e). Likewise, P-doped $g$-$C_3N_4$ micro-flowers composed of ultrathin nanosheets were obtained

by using phosphoric acid as the P source and cyanuric acid–melamine complex as the supramolecular precursor [97]. The inimitable porous micro-flower, with P doping and high surface area, enhanced the utilization of visible light and promoted isolation separation and mobility in the photogenerated charges, which promoted the $H_2$ rate by 24 times more than the bulk g-$C_3N_4$ flake-like structure. In addition to mesoporous P-doped g-$C_3N_4$ 3D nanoflower, one-dimensional P-doped hexagonal tubular carbon nitride (P-TCN) was reported in hydrothermal and pyrolysis processes using phosphorous acid and ME as raw materials [91]. As seen from the SEM image (Figure 5f) P-TCN had a hexagonal tube with the layered stack structure that comprised exposed rich pores of 40–60 nm along the tube wall as shown in the TEM image (inset in Figure 4f). According to the UV/Vis light absorption spectra and XPS valence band spectra, the electronic structure of P-TCN changed after P doping relative to bulk g-$C_3N_4$ (GCN); the corresponding band structure alignments are depicted in Figure 4g. Photoluminescence (PL) emission can be used to determine the trapping and transfer behavior of photoexcited charges. The PL intensity of P-TCN decreased significantly, indicating a lower recombination rate after P doping compared with GCN (Figure 5g) due to its hexagonal tube morphology, which provides a short path for the mobility of photogenerated charges and delays their recombination. Figure 5h presents the time course of HERs for GCN, TCN, and P-TCN, in which P-TCN displays the highest hydrogen evolution rate at 67 µmol h$^{-1}$ because of P doping and its tubular structure. To add, no noticeable deterioration of $H_2$ evolution rate was observed during four cycles of 20 h, suggesting the robust stability of P-TCN. During the linear sweep voltammetry (LSV) measurements (Figure 5i), the larger hydrogen evolution current density of P-TCN represented enhanced electron transfer compared to that of GCN. Additionally, P-TCN revealed an almost threefold enhancement in photocurrent response compared to GCN (Figure 5j). This implies the significant effect of porous hexagonal tube on boosting the specific surface area and active sites in addition to the effect of P doping on reducing band gap energy, enhancing the electric conductivity, and delaying the recombination of photogenerated electron–hole pairs, which lead to increment of the photocatalytic HER efficiency on P-TCN. A similar P-doped tubular g-$C_3N_4$ structure was also obtained via hydrothermal and thermal polymerization processes using ME and sodium pyrophosphate as starting precursors [92]. Afterwards, coral-like porous P-doped g-$C_3N_4$ tubes (PCNT) were developed by using dicyandiamide and phytic acid as starting materials [96]. The highest photocatalytic hydrogen evolution rate, 2020 µmol h$^{-1}$g$^{-1}$, was achieved on PCNT, which is about 4.7- and 22.4-fold compared to that of g-$C_3N_4$ tubes and pristine bulk g-$C_3N_4$, respectively. Additionally, Zhang et al. prepared P-doped macro/mesoporous g-$C_3N_4$ microrods (CNRs) by direct calcination of ethylene diphosphonic acid–ME complex fiber network [93]. Benefitting from unique morphology and electronic properties, the P-CNRs yield a 5.5 times higher hydrogen evolution rate than pristine g-$C_3N_4$.

In most cases, the doped P atoms only substitute C or N atoms of g-$C_3N_4$ to form either a P-N or P-C bond [99,147]. Zhou et al. proposed a thermally induced copolymerization route for P-doped g-$C_3N_4$ by using hexachlorocyclotriphosphazene as a phosphorus source and guanidinium hydrochloride as g-$C_3N_4$ precursor, respectively [90]. X-ray photoelectron spectra (XPS) and NMR results revealed that the P atoms locate at the corner and bay carbon sites of g-$C_3N_4$ network to form P-N bond, and the lone electron from the P atom delocalizes to the $\Pi$-conjugated triazine ring. The P doping could modify the electronic structure, surface texture, and electric conductivity of g-$C_3N_4$, leading to improved photocatalytic activity. In another study, Sun and his coworkers realized dual-site doping by using ammonium hypophosphite as the P source, thus regulating the band structure of g-$C_3N_4$, accelerating the charge separation and transfer [98]. Various characterization results indicate that two forms of P-N coordination exist: one is the substitution of carbon atoms in the tris–triazine framework to form P-N bonds, the other is the formation of surface N-P-O bonds. Consequently, the dual-site P-doped g-$C_3N_4$ yields a 5.7-fold higher $H_2$ evolution rate than the pristine catalyst.
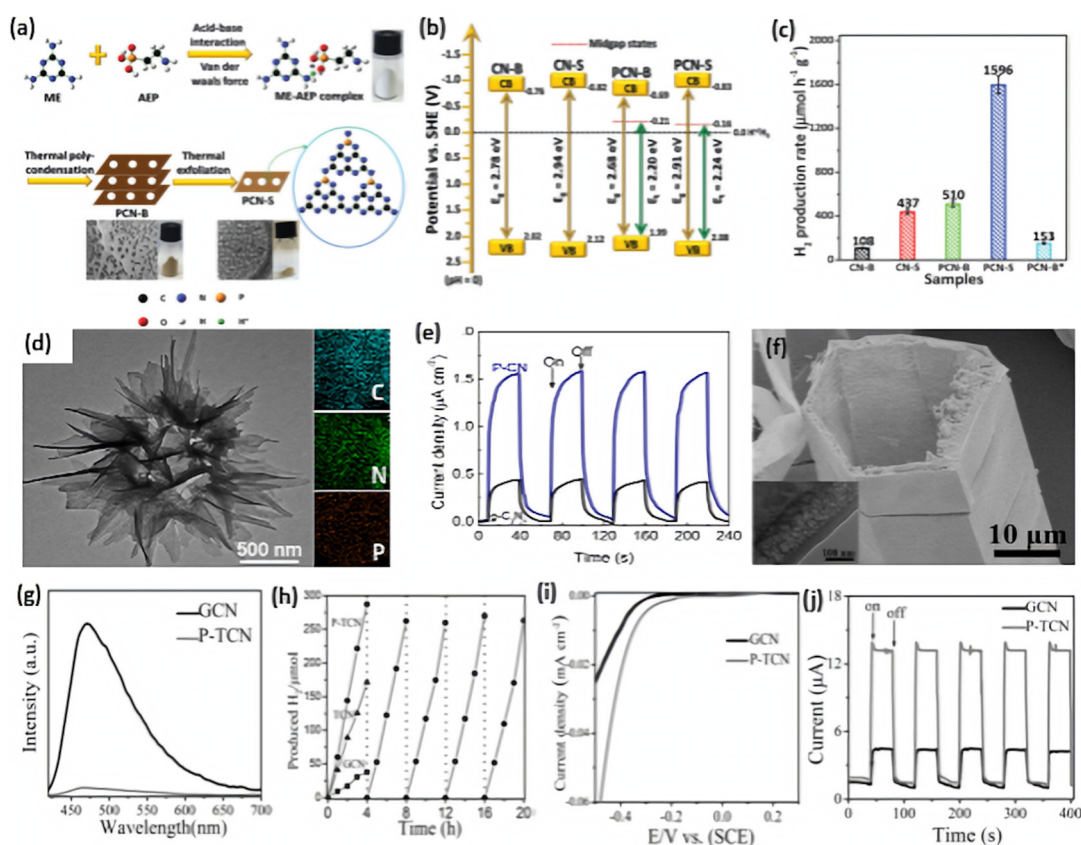
**Figure 5.** (**a**) Schematic illustration of the synthesis process of porous PCN-S. (**b**) Electronic band structures of CN-B, CN-S, PCN-B, and PCN-S. (**c**) The photocatalytic activity comparison of CN-B, CN-S, PCN-B, PCN-S, PCN-B*; adapted with permission from Ref. [89]. 2015, Royal Society of Chemistry. (**d**) Transmission electron microscope (TEM) image and EDS mapping of P-CN nanoflowers, beside its photocurrent–time curves relative to bulk g-$C_3N_4$ flakes (**e**); adapted with permission from Ref. [76]. 2015, American Chemical Society. (**f**) SEM and TEM images of P-TCN. (**g**) PL spectra of GCN and P-TCN. (**h**) Time course of $H_2$ production for GCN, TCN, and P-TCN. (**i**) Polarization curves of GCN and P-TCN. (**j**) Photocurrent–time curves for GCN and P-TCN; adapted with permission from Ref. [91]. 2016, John Wiley & Sons, Inc.

### 5.1.2. Sulfur Doping

Sulfur doping has also been used to tune the bandgap and electronic structure of g-$C_3N_4$ for enhanced visible light absorption, improved charge separation and transfer, and consequently, photocatalytic performance [104,107,111,148]. For instance, Xu's group fabricated S-doped mesoporous g-$C_3N_4$ (mpgCNS) by using thiourea as a precursor and $SiO_2$ nanoparticles as a template [113]. As evidenced by XPS study, the S atoms tend to replace carbon sites to form an S-N bond. Compared with undoped mesoporous g-$C_3N_4$ (mpgCN), mpgCNS can further enhance light absorption in both UV and visible light regions. Moreover, the lowest PL intensity for mpgCNS implies the less recombination tendency of photogenerated electron–hole pairs. As expected, the $H_2$ evolution rate of mpgCNS is 36% higher than that of mpgCN. Additionally, S-doped 2D graphitic carbon nitride nanosheets (2D-SCN) were prepared by the initial polycondensation of thiourea to in situ doped S into bulk g-$C_3N_4$ (denoted as SCN), followed by the thermal oxidation process, as illustrated in Figure 6a [108]. The bulk g-$C_3N_4$ (CN) and 2D g-$C_3N_4$ nanosheets (2D-CN) were synthesized using urea as a precursor. The thermal oxidation etching for different times 1, 2, and 3 h formed 2D-SCN-1h, 2D-SCN-2h, and 2D-SCN-3h, respectively. This led to a break in the hydrogen bond and reduced the thickness between the 2D layers of g-$C_3N_4$ nanosheets alongside the creation of a mesoporous structure. The TEM

image of 2D-SCN-3h showed well-defined mesoporous nanosheets with multiple pores (4.4–21.8 nm) (Figure 6b) with an average thickness of 4.0 nm as shown by atomic force microscope (AFM) (Figure 6c). The surface area, porosity (i.e., pore volume and pore diameter), and $H_2$ production increased significantly after oxidation etching. Thereby, the surface area (226.9 $m^2$/g) and pore volume (0.81 $cm^3$/g) of 2D-SCN-3h were superior to SCN by 13.66 and 6.23 times, respectively, due to their porous morphology. The XPS displays the presence of C, N, and S; meanwhile, the XPS spectrum of S 2p—in which the weak peak at 163.7 eV is related to the S-C bond by substituting lattice N (Figure 6d)—was not similar to the work mentioned above reported by Xu's group. As seen from the transient photocurrent response for three samples in Figure 6e, 2D-SCN-3h possesses a higher current density than SCN due to its porous nanostructure and great surface area that increases active sites, which is beneficial for more highly efficient charge separation. By comparing the photocurrent between 2D-SCN-3h and 2D-CN, it is also proven that S doping can promote charge carrier separation and transfer. According to partial density of states computation, the S-C-N bonds formed by S doping are more effective than O-C-N bond. S doping into a porous morphology can also narrow the band gap and enhance light absorption, thus synergistically improving photocatalytic performance. This is shown in the higher $H_2$ production rate (127.4 μmol/h) in 2D-SCN-3h than in 2D-SCN-2h (85.8 μmol/h), 2D-SCN-1h (9.7 μmol/h), 2D-CN (41.6 μmol/h), SCN (0.5 μmol/h), and CN (0.4 μmol/h) (Figure 6f). Zhou et al. further regulated the above polymerization process of thiourea by adding $NH_4Cl$ as a bubble template to obtain g-$C_3N_4$ with a porous network [106]. It is deduced that $NH_4Cl$ can decompose into $NH_3$ and HCl during polymerization, which contributes to the forming of a porous structure and avoiding agglomeration. Apart from thiourea, trithiocyanuric acid also acts as a widely reported sulfur-containing precursor for S doping [105,110,112]. Luo and his co-workers proposed a one-step thermolysis of thiocyanuric acid approach to preparing ultrathin S-doped holey g-$C_3N_4$ nanosheets [110]. The optimum sample can deliver a superior $H_2$ evolution rate of 6225.4 μmol $g^{-1}h^{-1}$ under visible light irradiation, almost 45-fold higher than pristine bulk g-$C_3N_4$. Additionally, an apparent quantum yield of 10% at 420 nm could be yielded. In addition to the nanosheets, nanoporous g-$C_3N_4$ microrods were prepared for photocatalytic HER by self-assembling melamine–trithiocyanuric acid supramolecule, followed by calcination [105].
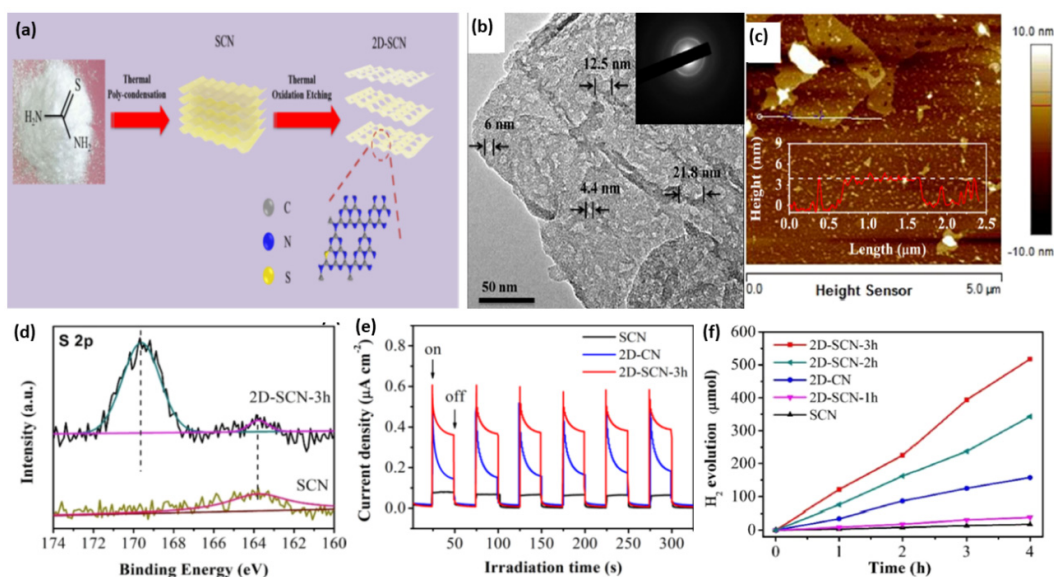


**Figure 6.** (**a**) Schematic illustration of the synthesis procedure of 2D-SCN. (**b**) TEM image and (**c**) AFM image of 2D-SCN-3h. (**d**) S 2p XPS spectra of SCN and 2D-SCN-3h. (**e**) Transient photocurrent–time curves, and (**f**) $H_2$ production on 2D-SCN-3h, 2D-SCN-2h, 2D-SCN-1h, SCN, 2D-SCN, and 2D CN. Adapted with permission from Ref. [108]. 2020, American Chemical Society.

### 5.1.3. Boron Doping

B-doped porous ultrathin g-$C_3N_4$ nanosheets (CNB NS) were prepared by the initial hydrothermal treatment of an aqueous solution of melamine and barbituric acid for 10 h at 180 °C, followed by annealing at 550 °C for 2 h [116]. In their synthesis, barbituric acid (BA) not only assemble with melamine to generate a porous structure but also replace the triazine ring of the heptazine unit in the g-$C_3N_4$ framework. As references, CNH was obtained via the hydrothermal and annealing methods but without barbituric acid and CN was synthesized by direct heating of melamine at 550 °C for 2 h. The SEM image of CNB NS showed the formation of porous nanosheets (Figure 7a) and the TEM image revealed that the nanosheets are ultrathin with multiple in-plane pores and curled edges (Figure 7b) with an average thickness of 3–4 nm (Figure 7c). This reflects the effect of annealing and hydrothermal treatment in presence of barbituric acid on the morphology as further seen by the BET surface area of CNB NS (55.07 m$^2$/g) being 3.26 times greater than CN (16.88 m$^2$/g). XPS analysis revealed the higher ratio of the C1s peak at 284.6 eV in CNB NS compared to in CN, owing to the incorporation of B-doping; however, the peak of the B-based dopant does not appear in the XPS survey and there is no other quantitative analysis to confirm presence of B. The UV-vis diffuse reflectance spectra (DRS) showed a red shift of the band edge absorption of CNB NS of 30 nm more than CN, implying that incorporating BA could decrease Π-deficiency and induce an asymmetric electron density. As reflected by the electronic band structure in Figure 7b, the conduction band of CNB NS shows a negative shift of 0.16 eV compared to that of CN, which implies the effect of a porous ultrathin curled nanosheet shape on reducing photoexcited electrons as seen in the lower band gap energy of CNBS (2.69 eV) than CN (2.78 eV), which is characteristic of the generation of photogenerated electron–hole pairs and delays their recombination. This is seen in the photocurrent–time curves, which indicate the quick and uniform photocurrent responses on all samples but with a superior activity on CNB NS (Figure 7d). The photocurrent responses were reversible under each dark/light circulation, which implied a higher photocurrent in light than under dark. Furthermore, CNB NS showed the highest hydrogen evolution rate at 1323.25 µmol h$^{-1}$g$^{-1}$, which is almost 13 times higher than that of CN (Figure 7e). This is due to its porous nanostructure with great surface area, which provides more exposed catalytic active sites along with the prevention of nanosheet aggregation during the HER as shown in the stability of CNB NS for five cycles without any apparent attenuation of the H$_2$ evolution rate. Figure 7f displays the wavelength-dependent apparent quantum efficiency (AQE) of H$_2$ evolution for CNB NS, and the AQE decreases with the increased wavelength due to the light-induced HER, implying enhanced visible light harvesting. In another study, B-doped carbon nitride nanotubes were fabricated by a simple hydrothermal treatment of boric acid and melamine, followed by calcination [117]. Although the band structure of carbon nitride was not changed after B doping, the fully exposed active sites and high-density charge carriers endowed them with a highly efficient and stable hydrogen evolution rate.

### 5.1.4. Oxygen Doping

Oxygen-doped g-$C_3N_4$ was first prepared using a facile H$_2$O$_2$ hydrothermal approach [122]. As evidenced by the XPS result, O atoms could be incorporated into the matrix and substitute sp$^2$-hybridized nitrogen atoms in g-$C_3N_4$ to form C-O and N-C-O species. Moreover, a negative shift in the conduction band minimum was observed after O doping, whereas the valence band maximum remained unchanged. As a result, the O doping could adjust the electronic and band structure, resulting in extended visible light response, enlarged surface areas, and suppressed charge carrier recombination. In another study, Huang et al. reported the synthesis of O-doped g-$C_3N_4$ with a porous network by condensation of supramolecular aggregates formed by melamine and H$_2$O$_2$ [123]. They found that the control over the O-dopant amount is significant, and excess dopants could serve as defect sites for electron–hole recombination. The optimal catalysts delivered 6.1 and 3.1 times higher HER activity than pristine and porous g-$C_3N_4$ and an apparent quantum efficiency

of 7.8% at 420 nm. Guo and his coworkers synthesized holey-structured g-C$_3$N$_4$ with edge oxygen doping using a photo-Fenton reaction in the presence of Fe$^{3+}$/Fe$^{2+}$ and H$_2$O$_2$. Based on the various characterization technique, oxygen edge doping can remarkably broaden light harvesting capacity and improve charge separation efficiency.
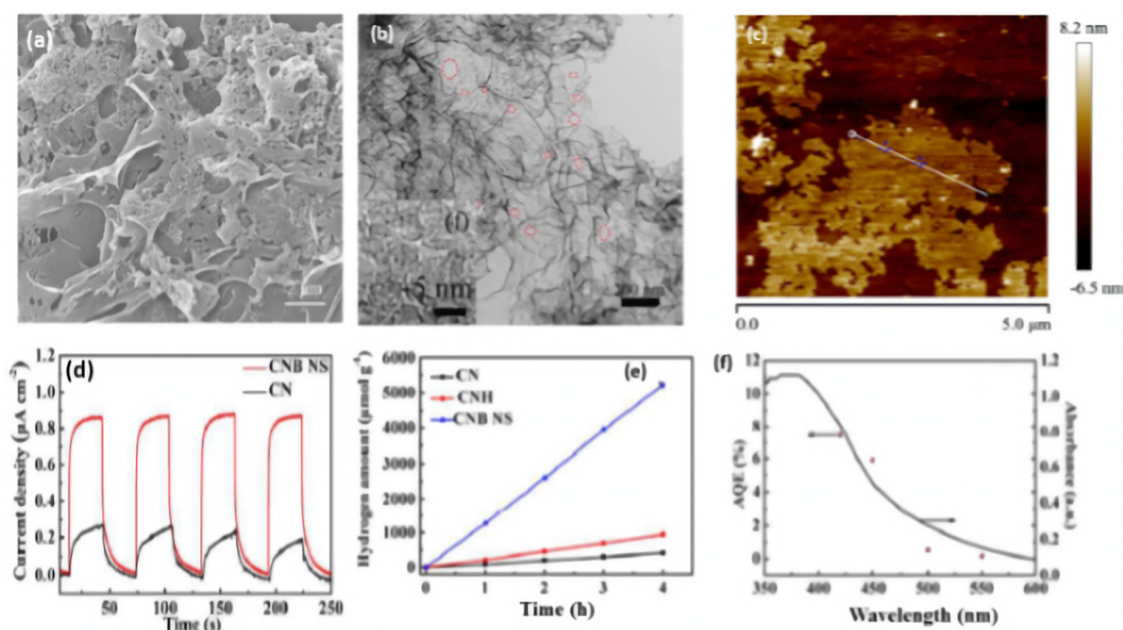


**Figure 7.** (**a**) SEM image, (**b**) TEM image, (**c**) AFM image of CNB NS. (**d**) Transient photocurrent–time curves, (**e**) H2 production amount on CNB NS, CNH, and CN nanocatalysts. (**f**) The wavelength-dependent AQE and absorption curve of CNBs. Reproduced with permission from Ref. [116]. 2018, Royal Society of Chemistry.

Apart from H$_2$O$_2$, Huang's group introduced ammonium persulphate ((NH$_4$)$_2$S$_2$O$_8$) into the co-pyrolysis and polycondensation process of g-C$_3$N$_4$ [127]. Owing to its strong oxidative ability, (NH$_4$)$_2$S$_2$O$_8$ can inhibit polycondensation from creating nitrogen defects and contribute to the porous structure and oxygen dopants. Importantly, the pathway of electron transition was changed with respect to bulk g-C$_3$N$_4$, which significantly accelerated the charge separation. As expected, nearly sixfold higher photocatalytic activity than pristine g-C$_3$N$_4$ was observed for O-doped g-C$_3$N$_4$. Another typical example is that Wu et al. developed multiple thermal treatment methods to obtain hollow O-doped g-C$_3$N$_4$ nanosheets (OCN) under a N$_2$/O$_2$ atmosphere [132]. The formation mechanism was attributed to the adsorption of the O atom in g-C$_3$N$_4$ under the initial thermal treatment of urea in the N$_2$/O$_2$ atmosphere to form OCN-1, which oxidized and allowed integration of more O-doping after being retreated thermally under the N$_2$/O$_2$ to form OCN-2 and then oxidized again to form OCN-3 and OCN-4 (Figure 8). The same concept could be feasible for allowing the doping of other atoms with O via simple mixing with sources for heteroatoms (i.e., thiourea and boron trichloride). Meanwhile, bulk g-C$_3$N$_4$ (MCN) was synthesized under identical conditions with OCN-1 except for using melamine under an argon atmosphere. The TEM image (Figure 9a) and AFM image (Figure 9b) of OCN-3 showed the formation of porous monolayered nanosheets with uniform distribution of abundant pores (25 nm size) and the thickness of the sheet was ~0.45 nm. The surface area, porosity, and O-content increased with increasing the thermal treatment times, but the OCN-3 possessed the highest surface area of (148.50 m$^2$/g$^1$) compared to OCN-2 (102.84 m$^2$/g$^1$) and OCN-1 (97.88 m$^2$/g$^1$); the high surface area of OCN-3 is beneficial for promoting the HER. XPS analysis revealed that the O content increased from 0.84 at% in OCN-1 to 1.62% in OCN-3 and 2.07% in OCN-4. The photocurrent response revealed that OCN-3 had a higher photocurrent density (0.35 μA/cm$^2$) than that of OCN-1 (0.14 μA/cm$^2$) and OCN-2

(0.26 μA/cm$^2$) (Figure 9c) in addition to durability for five cycles over 20 h with only 10.4% loss, but the current density was very low in all samples and the difference between the photocurrent and electrochemical current was inferior. Under visible light irradiation for 5 h, the hydrogen evolution activity of OCN-3 is the highest among these catalysts (Figure 9d). The quantum yield of OCN-3 decreases with increased wavelengths, and it can reach 26.96% at 400 nm and 4.28% at 420 nm (Figure 9e) due to the ability of OCN-3 to induce the generation of electron–hole pairs along with delaying their recombination. This is shown in the electron spin resonance spectroscopy (ESR) analysis with TEMPO, which showed that OCN-3 had a weak signal that is an inaction for a large number of photo-exited electron–hole pairs relative to OCN-1 and OCN-2, implying the significant effect of porous monolayer sheet morphology and higher O-doping (Figure 9f,g). That the signals for electron–hole pairing under light irradiation reduced more slowly over time than its counterparts is evidence of the efficient isolation of photo-exited radicals. Density functional theory was applied to clarify the enhanced photocatalytic mechanism of O atoms. Based on the density of states, the band gap of pure g-C$_3$N$_4$, O-adsorbed g-C$_3$N$_4$, and O-doped g-C$_3$N$_4$ is about 2.58, 2.55, 2.16 eV, respectively (Figure 9h–j). Thus, it can be concluded that introducing oxygen atoms can narrow the band gap for harvesting more visible light, promoting the generation and isolation of electron–hole pairs, while porous nanosheets with high surface area provide more accessible active catalytic sites and accelerate the charge mobility and diffusion of reactants or products during the HER.
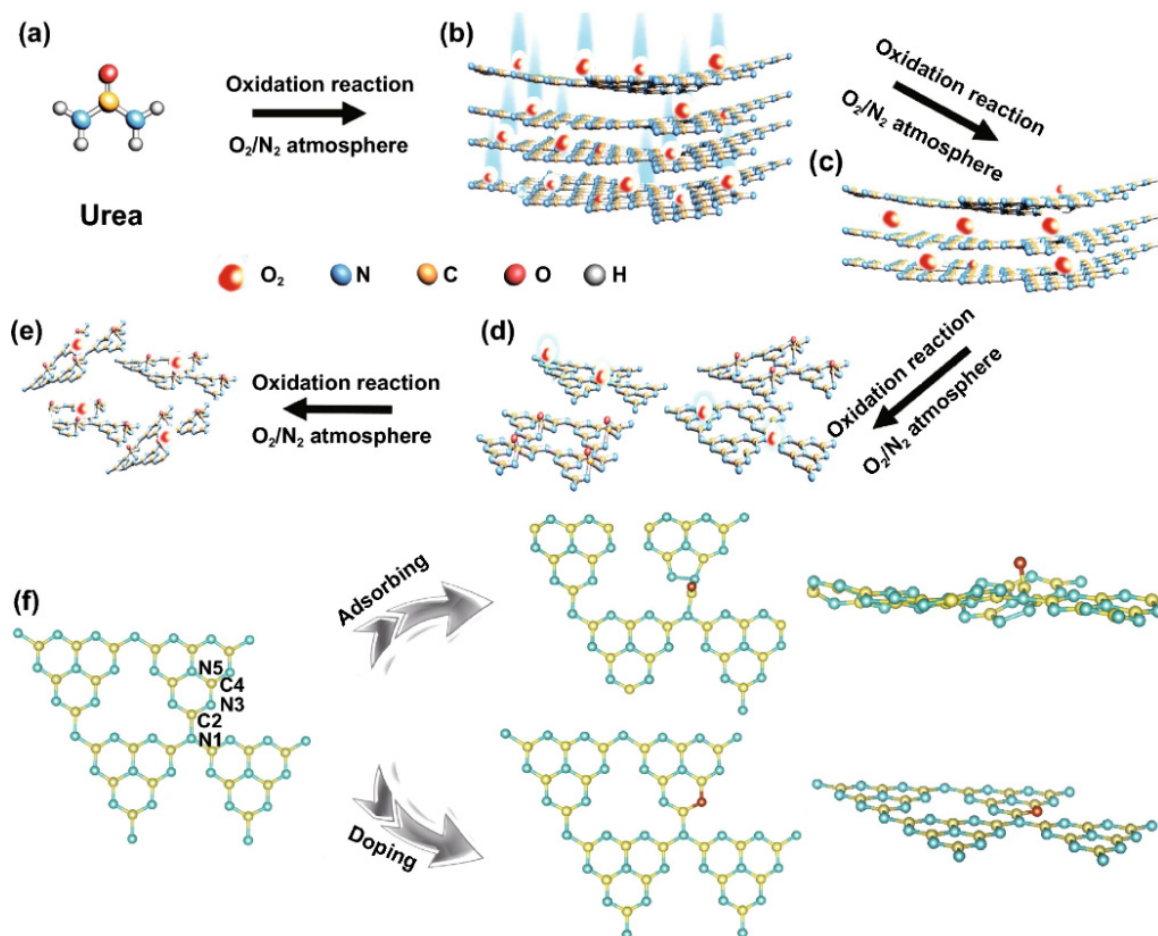


**Figure 8.** The formation process and mechanism of OCN photocatalysts. (**a**–**e**) synthesis of OCN photocatalysts. (**f**) DFT simulations. Reprinted with permission from Ref. [132]. 2021, Springer Nature Switzerland.
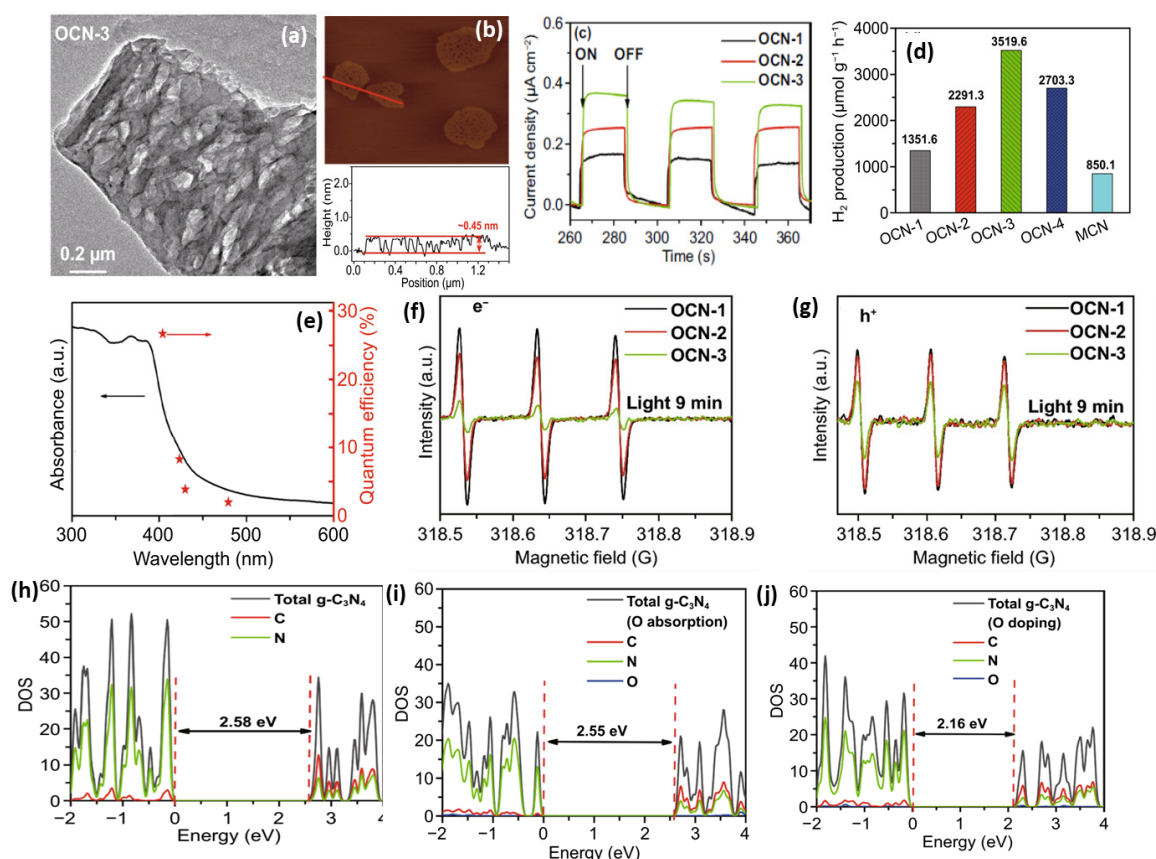
**Figure 9.** (**a**) TEM, (**b**) AFM image of OCN-3. (**c**) Transient photocurrent responses and (**d**) $H_2$ production rate under optical filter ($\lambda > 420$ nm) of OCN-1, OCN-2, and OCN-3. (**e**) The QE–wavelength curve of OCN-3. (**f**) ESR of electron and (**g**) hole on OCN-1, OCN-2, and OCN-3. The density of state of (**h**) bare g-$C_3N_4$, (**i**) O-doped g-$C_3N_4$, and (**j**) O-CN. Adapted with permission from Ref. [132]. 2022, Elsevier Inc.

### 5.1.5. Carbon Doping

Li et al. proposed a facile microwave-assisted heating approach to yield C-incorporated g-$C_3N_4$ by copolymerizing $\Pi$-electron-rich barbituric acid with melamine [135]. Theory calculations showed that carbon incorporation provides more available $\Pi$-electrons, shortens the bandgap, and in addition, microwave irradiation could improve the crystallinity of g-$C_3N_4$, benefiting the rapid charge transfer. The $H_2$ production amount of C-incorporated g-$C_3N_4$ is almost 20 times higher than that of g-$C_3N_4$ synthesized by the conventional heating method. Chen and coworkers realized the simultaneous introduction of carbon atoms and nitrogen vacancies in g-$C_3N_4$ by a combined hydrothermal–conjugate–copolymerization strategy [136]. Three important features were mentioned: (1) the porous structure could provide more available active sites for reaction species adsorption, (2) the defects-induced midgap could broaden the visible light absorption, (3) the gradient C-doping could promote charge carrier transfer, enabling excellent photocatalytic activity for C-doped g-$C_3N_4$.

Given the unique structural advantage, 1D porous strip-like carbon nitride was prepared by calcining supramolecular precursor (Nic-M) formed by molecular self-assembly of melamine and nicotinic acid (Figure 10a) [138]. The SEM image (Figure 10b) of Nic-CN exhibits a strip nanostructure morphology with about 1 μm width; meanwhile, Nic-M preserved strip-like morphology well (Figure 10c). The TEM image (Figure 10d) shows the thinner strip features of Nic-CN with pores distributed on the surface, which can benefit the photocatalytic reaction. The XPS and elemental analysis confirmed the C-doping as shown by the higher C content in Nic-CN (47.06%) than PCN (45.14%). The UV-vis DRS (Figure 10e) showed the adsorption peak at 200–400 nm with a band edge extended to

nearly 460 nm in PCN and 460–700 nm in Nic-CN, due to the 1D porous strip-like morphology and modification of pyridine groups. This led to broadened optical absorption of Nic-CN by a threshold of up to 700 nm more than PCN and enhanced the separation efficiency of photogenerated electron–hole pairs. Moreover, the extended conjugation resulted in a downshift of the conduction band edge and, thus, a narrower bandgap of Nic-CN 2.65 eV than PCN (2.71 eV). Compared with PCN, the lower PL peak intensity of Nic-CN suggests inhibitive recombination and enhanced separation of carriers (Figure 10f). The transient state PL spectra show the shorter lifetime of Nic-CN, which implies the faster transfer of photogenerated charge pairs and efficient separation of charge carriers. Thereby, the photocurrent responses of Nic-CN were higher and quicker than of PCN, implying superior transport (Figure 10g). The photocurrent density of Nic-CN was higher than that of dark current by nearly (1.5 times). Unexpectedly, a nearly 18 times higher hydrogen evolution rate (126.2 $\mu$mol h$^{-1}$), was achieved for Nic-CN than that for PCN, due to its porous 1D strip-like shape with high surface area, more exposed and accessible active sites, as well as better optical absorption during the HER. This is shown in the higher surface area of Nic-CN (40.95 m$^2$/g) being four times more than PCN. In another report, carbon doping carbon nitride with a hollow tubular structure was fabricated for enhanced photocatalytic performance via a simple hydrothermal calcination method by using melamine and sodium alginate as precursors [139].
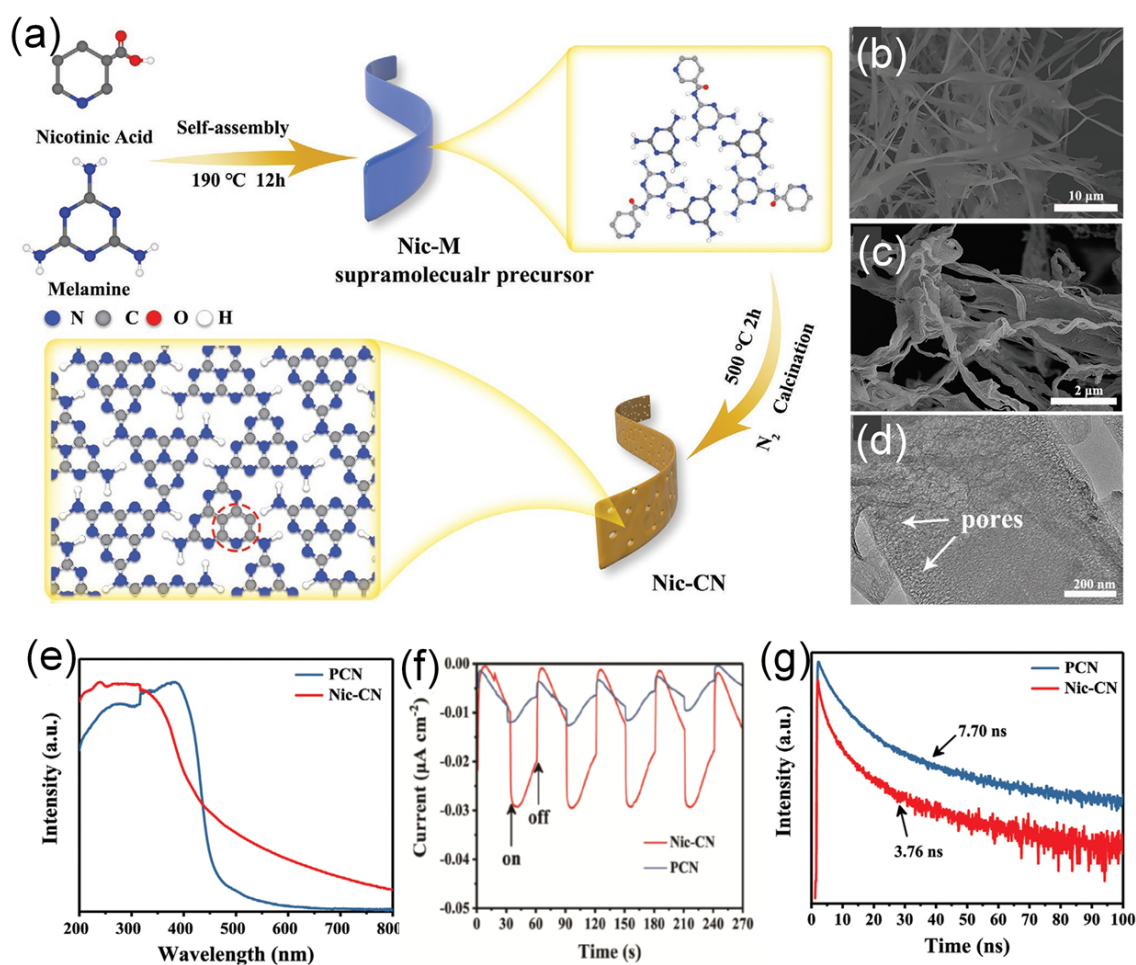


**Figure 10.** (**a**) Schematic illustration of the synthesis process of Nic-CN. SEM image of (**b**) Nic-M precursor and (**c**) Nic-CN. (**d**) TEM image of Nic-CN. (**e**) UV-vis DRS of PCN and Nic-CN, (**f**) transient photocurrent responses of PCN and Nic-CN, and (**g**) transient state PL spectra of PCN and Nic-CN. Adapted with permission from Ref. [138]. 2021, John Wiley & Sons, Inc.

### 5.1.6. Nitrogen Doping

The co-thermal condensation of a precursor with a nitrogen-rich additive is a common way of preparing N-doped g-C$_3$N$_4$ [140,142]. For instance, Fang et al. reported nitrogen self-doped graphitic carbon nitride for the first time by using melamine pretreated with hydrazine hydrate as the starting material [140]. The N/C mass ratio of 1.68 for the typical sample determined by elemental analysis was higher than that of 1.60 for g-C$_3$N$_4$ synthesized with melamine, indicating successful nitrogen incorporation. The as-prepared catalysts yielded nearly 14 times higher H2 evolution activity than pristine g-C3N4. Similarly, Shi's group prepared N-doped porous g-C3N4 nanosheets by calcining urea and N-N dimethylformamide (DMF) [124]. DMF not only affords a N source for N doping but also releases dimethylamine to generate pores in the g-C$_3$N$_4$ framework. Nitrogen-rich carbon nitride nanotubes (CNNTs) were fabricated via the thermal polycondensation of supramolecular intermediates [141]. On one hand, their hollow tubular structure can provide more active sites for light adsorption and more refraction pathways for charge separation. On the other hand, N atoms with larger electronegativity doping could attract more electrons for photogenerated charge carrier transportation.

### 5.1.7. Halogen Doping

It is well accepted that halogen doping of g-C$_3$N$_4$ can narrow the band gap, expedite the transfer of photogenerated electron–hole pairs, and enlarge specific surface areas, thereby improving its photocatalytic properties [143–146]. Wen's group proposed a universal route to synthesizing halogen (e.g., Cl, F)-doped g-C$_3$N$_4$ for enhanced photocatalytic hydrogen evolution performance [144]. They found that the F or Cl atom with a higher electronegativity tends to replace the N atom and bond to the C atom. Among them, ultrathin Cl-doped g-C$_3$N$_4$ nanostrips possess the strongest light absorption, a narrow band gap, larger specific surface areas, and faster charge separation and migration, thus delivering an excellent H$_2$ evolution rate of 5976 $\mu$mol h$^{-1}$g$^{-1}$. Gao et al. studied carbon nitride's iodine surface modification and doping by heating the self-assembly precursors formed by urea and ammonium iodide [145]. As an electron donor, iodine doping could increase the electron density in carbon nitride networks and tune their band structure. Moreover, the surface iodine could bond with positively charged holes to hinder the recombination of photogenerated charge pairs.

### 5.2. Binary Heteroatom-Doped Porous Carbon Nitride

Binary heteroatom doping could integrate the advantage of a single dopant, thus synergistically benefiting the photocatalytic activity [149–159]. The detailed structure and performance comparison of binary heteroatom-co-doped gCN-based catalysts is listed in Table 7. Additionally, the effect of morphology, preparation methods, and light source on the H$_2$ production rate and stability on binary doped porous gCNs is summarized in Table 7.

Cui et al. prepared B- and F-co-doped g-C$_3$N$_4$ via thermal polymerization of dicyandiamide, urea, and ionic tetrafluoroborate liquids, followed by post-annealing treatment [150]. The B atoms mainly located in the inside skeleton of g-C$_3$N$_4$, whereas F atoms existed in the surface layer. It was found that inner B doping contributes to enhancing visible light absorption and generating uniform porous structures during post-calcination treatment. Afterward, the same group reported the synthesis of porous C-I-co-doped carbon nitride with a similar method except for using an iodized ionic liquid as a precursor [153]. In another study, boron/oxygen-co-doped g-C$_3$N$_4$ nanomesh was obtained by a two-step doping and etching approach [151]. The as-prepared sample possessed a two-dimensional porous structure with a specific surface area of 160.58 m$^2$ g$^{-1}$.

Moreover, doped B and O atoms can regulate the band gap. Owing to the synergistic effect of the nanomesh-like structure and B- and O-co-doping, the light absorption ability and charge separation efficiency of g-C$_3$N$_4$ were enhanced. As a result, they displayed an excellent H$_2$ evolution rate of 9751 $\mu$mol h$^{-1}$g$^{-1}$ under visible light illumination, which is

almost 28 times higher than bulk g-C$_3$N$_4$. More importantly, the H$_2$ evolution activity kept over 20 h, revealing its robust stability. Dai's group proposed a facile approach to prepare C- and P-co-doped g-C$_3$N$_4$ (CPCN-1*) by the first self-assembly of melamine with phytic acid (denoted as CPCN-1), followed by hydrothermal treatment [154]. For comparison, pristine g-C$_3$N$_4$ (CN) was synthesized under identical conditions with CPCN-1 other than phytic acid, and CN* was obtained after hydrothermal treatment of CN. The SEM image of CPCN-1*, showed the formation of porous granular morphology (Figure 11a) with a rough surface and curled edges (Figure 11b); meanwhile, element mapping analysis revealed the presence of C, N, O, and P (Figure 11c–f). The surface area CPCN-1* (141.1 m$^2$/g) was significantly higher than that of CN (24.9 m$^2$/g) CN* (75.7 m$^2$/g) and CPCN-1 (44.8 m$^2$/g), due to the porous morphology and co-doping effect. Apparently, C and P doping could not change the band gap significantly but decreased the conduction band position of CPCN-1 and CPCN-1* in comparison with that of CN and CN*, implying much-enhanced photo-reducibility after co-doping (Figure 11g). Thus, CPCN-1 and CPCN-1* allowed for efficient improvement in the transfer of photogenerated electron–hole pairs over undoped CN and CN* because the dopants acted as trapping sites to restrain the combination of charge carriers. XPS analysis showed that the content of P dopants was found to be 0.29% in CPCN-1 compared to 0.14% in CPCN-1*. The H$_2$ production rate on CPCN-1* (1493.3 μmol h$^{-1}$g$^{-1}$) was 2.24, 2.34, and 9.7 times that of CPCN-1 (663.7 μmol h$^{-1}$g$^{-1}$), CN* (637.6 μmol h$^{-1}$g$^{-1}$), and CN (153.9 μmol h$^{-1}$g$^{-1}$), respectively (Figure 11h). This implies porous morphology with a higher surface area and co-doping lead to high optical adsorption, efficient charge transport, and great photoinduced reducibility. Moreover, CPCN-1* showed high stability over four cycles for 13 h. The photocurrent responses over five on–off cycles revealed the obvious enhancement in the current density under light than under dark with reversible behavior and the photocurrent intensity remained stable during the five cycles, but CPCN-1* was the most active (nearly eight times CN) (Figure 11i). Beyond the above observation, the integration of binary heteroatom-doping and a heterojunction structure into g-C$_3$N$_4$ was also realized for enhanced photocatalytic performance [155,160].



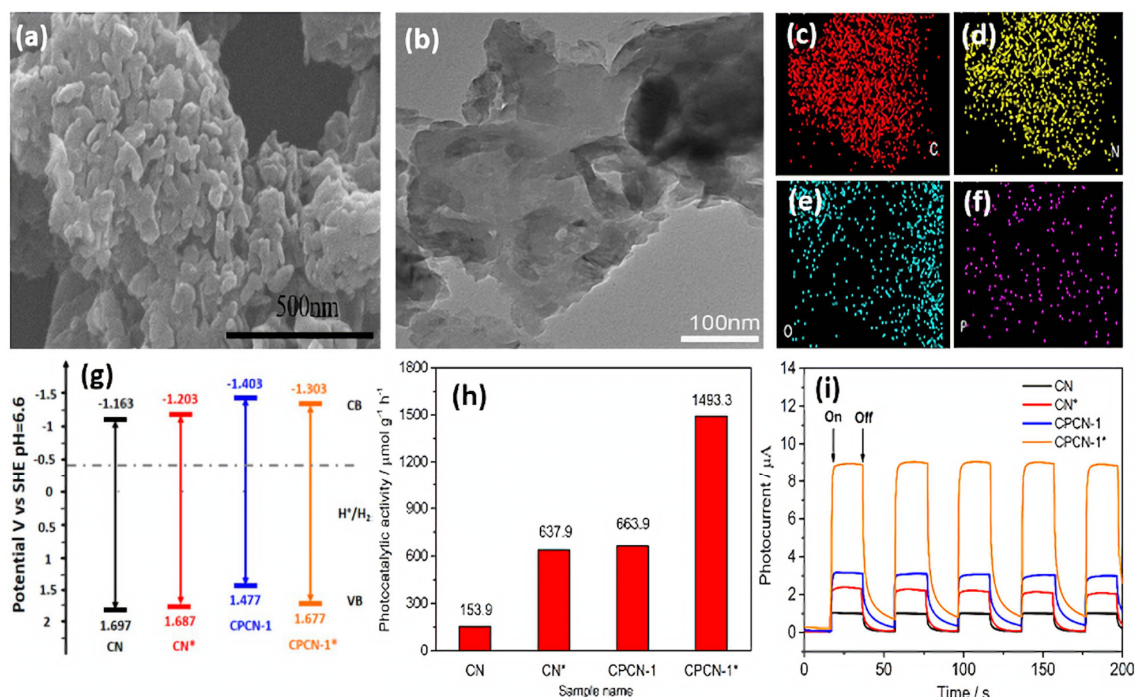**Figure 11.** (**a**) SEM image, (**b**) TEM image, and (**c–f**) element mapping analysis of CPCN-1*. (**g**) Electronic band gap structure, (**h**) H$_2$ production rate, and (**i**) transient photocurrent responses of CN, CN*, CPCN-1, and CPCN-1*. Adapted with permission from Ref. [154]. 2017, American Chemical Society.

**Table 7.** Comparison of photocatalytic performance of binary heteroatom-co-doped porous carbon nitrides toward HER.

| Photocatalysts | Dopants | Morphology | Synthetic Method | Co-Catalyst | Light Source | H$_2$ Evolution Rate ($\mu$mol h$^{-1}$g$^{-1}$) | Apparent Quantum Efficiency | Durability | Refs |
|---|---|---|---|---|---|---|---|---|---|
| r-CN-B/F | B, F | Dense aggregated microstructures comprising irregular nanosheets | Post-thermal treatment of B/F co-doped carbon nitride obtained from direct condensation using ionic liquid as dopant | 3 wt% Pt | Visible light irradiation ($\lambda > 400$ nm) | 6870 | | High H$_2$ evolution remains in the consecutive four runs | [149] |
| p-CN-BF | B, F | Small particles composed of porous nanosheets | In situ B and F co-doping using [Emin]BF$_4$ as dopants followed by post-calcination in air | 3 wt% Pt | 300 W Xe arc lamp | 7020 | | Only slight decrease observed in H$_2$ evolution after several cycles | [150] |
| BO-C$_3$N$_4$ | B,O | Porous nanomesh | Two-step doping and etching | 3 wt% Pt | 300 W Xe arc lamp equipped with a cutoff filter ($\lambda \geq 420$ nm) | 9751 | 8.1% at 420 nm | There was no obvious deactivation over 20 h | [151] |
| CNBS | B,S | Nanosheets composed of nanoholes and rupture | Co-pyrolysis of boric acid, thiourea and melamine in the muffle furnace | 1 wt% Pt | 150 W Xenon lamp with a 420 nm cutoff filter | 2660 | | No decrease in hydrogen production rate during long-time photocatalytic measurement up to five runs | [152] |
| CNIN$_{0.2}$ | C,I | Unconsolidated porous accumulation | In situ co-doping with iodized ionic liquid followed by post-thermal treatment in air | 3 wt% Pt | 300 W xenon-lamp with appropriate cutoff filter | 3364 | | Almost negligible deactivation could be observed after four consecutive cycles | [153] |
| CPCN-1* | P,C | Granular morphology | Self-assembly melamine with phytic acid, followed by hydrothermal treatment | 1 wt% Pt | 300W Xe lamp | 1493.3 | 2.14% at 420 nm | The H$_2$ generation rate recovered to initial value over three cycles | [154] |
| PSCN | P,S | Layered structure | One-step high-temperature polymerization | 3 wt% Pt | 300 W Xenon lamp with an UV-cutoff filter > 400 nm | 1969 | | The hydrogen evolution was not apparently attenuated following three cycles' running | [155] |
| PACN | P,O | Spiral nanotube | Phytic acid-assisted supramolecular self-assembly method | Pt | 5 W LED lights | 6437.65 | | PACN exhibited excellent recycling stability in four runs and maintained 95.20% of the primitive value of hydrogen evolution after four runs | [156] |
| CNB | C,O | Wrinkled nanosheets | Hydrothermal method using dicyandiamide, cyanuric acid and cyanobenzene as precursors | 3 wt% Pt | 300 W Xe-lamp with a 420 nm cutoff filter | 2595.4 | 16.6% at 420 nm | The photocatalytic activity decreased slightly after five cycles and no noticeable change of microstructure could be found | [157] |
| POCN-10 | P,O | Nanosheet | One-step thermal copolymerization of melamine and ammonium polyphosphate | 5 wt% Pt | 300 W Xenon lamp equipped with a 400 nm cutoff filter | 1588 | | No apparent decline of H$_2$ evolution activity by cycling three times in 12 h | [158] |
| SPCN0.1 | S,P | Porous microtube | Using melamine and ammonium dihydrogen phosphate as precursors | 3 wt% Pt | 300 W Xe lamp equipped with optical cutoff filter ($\lambda > 420$ nm) | 4200.3 | 10.3% at 420 nm | The performance did not significantly decrease after 12 h of experiment | [159] |

### 5.3. Ternary Heteroatom-Doped Porous Carbon Nitride

It has been proven that ternary heteroatom doping can show higher photocatalytic activity and unusual physiochemical properties with respect to binary and single heteroatom doping. For instance, Liu and coworkers realized the simultaneous doping and exfoliation of g-$C_3N_4$ by fabricating S-, P-, and O-co-doped ultrathin nanosheets via a facile annealing method [161]. As displayed in Figure 12a, S- and P-co-doped g-$C_3N_4$ (denoted as CN-SP) was first obtained by thermal condensation of the mixed precursors of melamine, thiourea, and diammonium phosphate. Subsequently, the CN-SP was annealed in the air for O doping; meanwhile, it could be exfoliated into ultrathin nanosheets (denoted as CN-SPO). The TEM image of CN-SPO ultrathin (~3 nm) exfoliated nanosheets morphology with sharp edges flat surface (Figure 12b), while CN and CN-SP had thicker tightly stacked sheets. The EDX analysis of CN-SPO clearly warranted the coherent distribution of C, N, S, P, and O, but the exact content is not mentioned in the manuscript (Figure 12c–g). Moreover, the XPS analysis of CN-SPO displayed the presence of C, N, S, P, and O. Experimental and theoretical results demonstrated that the S atoms occurred on the interstitial sites, whereas P and O atoms substituted C and N atoms, respectively. S, P, and O doping can probably create a more favorable charge transfer channel and boost charge migration. Accordingly, CN-SPO displayed the highest photocurrent response (8 $\mu A/cm^2$), compared to CN-SP and CN, implying the significant effect of S/P/O doping on the optimal separation rate of photogenerated carriers under visible light irradiation (Figure 12h). This is seen in the ESR analyses, which displayed a lower TEMPO-$e^-$ and TEMPO-$h^+$ TEMPO with three peaks (with ratio of 1/1/1) but with a less intensity on CN-SPO than CN under light than under dark (Figure 12i,j). This implied the superior reactivity of photoinduced charge carriers on CN-SPO. In addition, the narrow band gap and negatively shifting conduction band edge caused by heteroatom doping could broaden visible light absorption and enhance electron reducibility. As a result, an optimal $H_2$ evolution rate of (2480 $\mu mol\ g^{-1}\ h^{-1}$) was observed for CN-SPO, which was superior to CN (465 $\mu mol\ g^{-1}\ h^{-1}$) by five times. This is due to the tri-dopant, which promoted the photoexcited electrons transfer through the (O-P-C-$N_2$-S-$N_2$ or $N_2$-S-$N_2$-$C_1$-P-O) chain among the two adjacent heptazine units, which eased the isolation of the photogenerated carriers.

N-, P-, and O-co-doped carbon (NPOC)-filled CN microtubes (NPOC@CN) were synthesized via the initial mixing of urea and melamine with the poly(cyclotriphosphazene-*co*-phloroglucinol) (PCPP) microspheres and then hydrothermal and annealing too (Figure 13a). A 3, 5, and 7% amount of PCPP was used for preparation of 3%-NPOC@CN, 5%-NPOC@CN, and 7%-NPOC@CN, correspondingly. The high angle annular dark field (HAADF) image of 5%-NPOC@CN revealed a porous microtube structure with multiple pores (mesopore, micropore, and macropores) with the highest specific surface area of (68.75 $m^2/g^1$) (Figure 13b). The EDX mapping displayed that the atomic contents of C, N, O, and P are 66.05, 31.20, 2.59, and 0.15%, respectively (Figure 13c). The bandgap energy of 5%-NPOC@CN (2.18 eV) was lower than that of 7%-NPOC@CN (2.31 eV), 3%-NPOC@CN (2.43 eV), and CN (2.63 eV), implying better light harvesting and isolation efficiency of photogenerated carriers due to the tri-dopant effect. Furthermore, the $H_2$ production rate on 5%-NPOC@CN (1149.71 $\mu mol\ g^{-1}\ h^{-1}$) was 1.32, 1.58, 2.06, and 112.60 times greater than that of 7%-NPOC@CN (869.13 $\mu mol\ g^{-1}\ h^{-1}$), 3%-NPOC@CN (724.43 $\mu mol\ g^{-1}\ h^{-1}$), CN (556.89 $\mu mol\ g^{-1}\ h^{-1}$), and bulk CN (10.21 $\mu mol\ g^{-1}\ h^{-1}$), respectively. This is also shown in the quicker response and higher photocurrent density of 5%-NPOC@CN than its counterpart (Figure 13d). All samples showed a noticed difference between photocurrent and electrochemical current. Thereby, tri-doping could pave the way for creation of novel CN-based photocatalysts for HER, but it is rarely reported and should be explored.
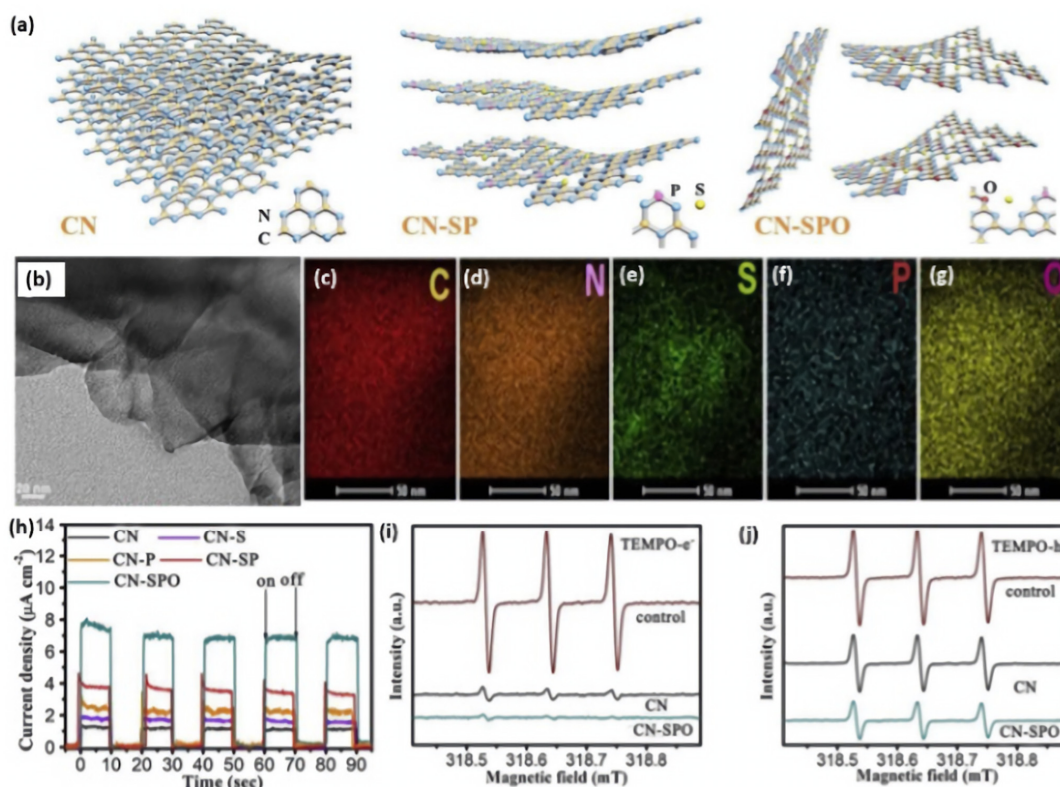
**Figure 12.** (**a**) Schematic illustration of exfoliation process of CN, CNSP, and CN-SPO. (**b**) TEM image and (**c–g**) EDX mapping of CN-SPO. (**h**) Transient photocurrent responses of CN-SPO and its counterparts. (**i**) ESR of electron and (**j**) hole of CN-SPO and CN. Adapted with permission from Ref. [161]. 2019, Elsevier Inc.
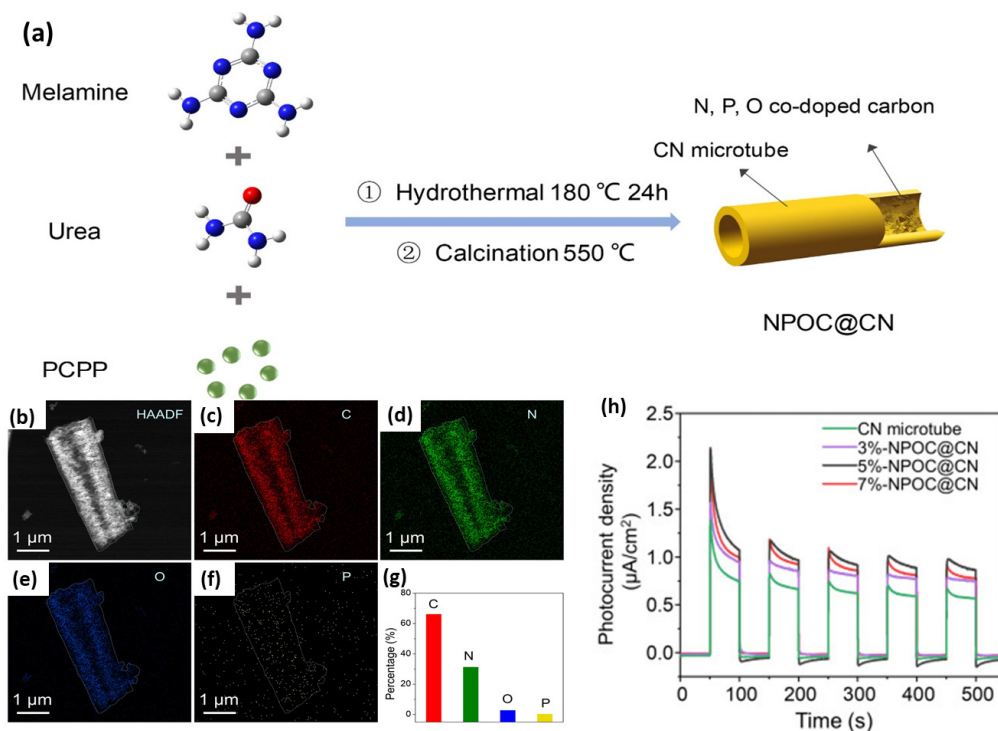


**Figure 13.** (**a**) The formation process, (**b**) HAADF-STEM, (**c–g**) EDX mapping of 5%-NPOC@CN. (**h**) transient photocurrent responses on 5%-NPOC@CN relative to its counterparts. Adapted with permission from Ref. [162]. 2022, Elsevier Inc.

## 6. Conclusions and Prospective

This review highlighted the synthesis of non-metal-doped porous gCNs for the photocatalytic HER. This includes the utilization of $H_2$ as a fuel and its storage in addition to the fundamentals related to water electrolysis and the photocatalytic HER process (i.e., mechanism, measurements, and calculation) and non-metal dopant configuration into gCNs. Meanwhile, the effect of non-metal dopants (i.e., mono, binary, and ternary heteroatom (i.e., P, O, S, N, and B)-doped porous gCN nanostructures on the enhancement of photocatalytic $H_2$ production were also discussed as a function of photocatalyst shape, composition, bandgap, and electrolyte type or concentration on HER activity and durability.

Mono-non-metal-doped porous gCNs are studied more than binary-doped, while ternary-doped gCN is rarely reported; however, mono-doped gCNs are the most active and promising for the HER. B-CNNT obtained via the hydrothermal and calcination of method in the presence of boric acid revealed a $H_2$ rate of (22,100 µmol $h^{-1}g^{-1}$) [117] relative to CNNTs formed via the supermolecule self-assembly method that showed a $H_2$ rate of (18,060 µmol $h^{-1}g^{-1}$) [141], and PCNNFs fragmented nanoflakes obtained via doping and annealing of biomass (15,921 µmol $h^{-1}g^{-1}$) [95]. Binary BO-$C_3N_4$ formed via a two-step doping and etching method is among the most promising photocatalysts for HERs, with a $H_2$ evolution rate of (9751 µmol $h^{-1}g^{-1}$) [151] in addition to high durability for 20 h. Moreover, p-CN-BF obtained via in situ co-doping using [Emin]$BF_4$ and calcination in air yielded a $H_2$ rate of (7020 $h^{-1}g^{-1}$) [150]; however, both materials needed Pt as a co-catalyst. Ternary CN-SPO showed a $H_2$ evolution rate of (2480 µmol $g^{-1}$ $h^{-1}$) [161] due to the presence of S atoms on the interstitial sites and substitution of C with P and N atoms with O atoms in gCN, resulting in lower bandgap and higher light absorption efficiency. The supramolecular self-assembly of multiple nitrogen-enriched carbon precursors such as melamine with cyanuric acid [105] and urea with ammonium iodide [145] are effective in the formation of porous gCN nanostructures with high surface area. This is in addition to facilitate in situ doping with non-metal atoms during the self-assembly process (i.e., S-doping in case of self-assembly of thiourea, O doping using cyanuric acid, and B doping using boric acid). Although there has been substantial progress made in the synthesis of porous, doped gCN photocatalysts for HERs, they remained impractical for large-scale applications and various perspectives and barriers are still unaddressed:

- Previous porous, doped gCNs in the form of 2D nanosheets and other porous nanostructures are rarely reported or not yet reported. Porous multidimensional doped gCN (i.e., nanoflower, nanodendrite, yolk–shell, and nanocage) and one-dimensional (i.e., nanowires, nanotubes, nanorods, and nanotubes) morphologies are imminent with their impressive characteristics (i.e., high electrical conductivity, great surface area, abundant defects, massive active/accessible active sites, stabilization of metal/non-metal atoms, and maximized atomic utilization) [163]. These merits can endow the HER activity and the durability of doped porous gCNs. Such porous nanostructures could be synthesized using multiple nitrogen-rich carbon precursors containing non-metal elements (i.e., melamine, thiourea, cyanuric acid, and cyanimide) and changing the preparation conditions (i.e., annealing environment, templates, and solvent type) [28,163]. Meanwhile, the reported g-doped porous gCNs are powder, which cannot be used directly in electrolysis and require several steps to be used as a cathode. This could be realized via the in situ fabrication of gCNs on solid carbon-cloth sheets or metal hydroxide/oxide substrate that could be used as a cathode for the HER.

- Particular attention should be paid to developing facile, one-step, and eco-friendly methods to fabricate g-$C_3N_4$ with various morphologies. Recently, our group developed a simple, template-free, one-pot approach for the fabrication of porous one-dimensional gCN nanostructures (i.e., wires, fibers, tubes, and rods) in situ, doped with various metals (i.e., Au, Pd, Pt, Cu, and their combinations) with high surface area and outstanding catalytic properties for CO oxidation [3–5,164]. The same tactics can be extended to prepare other gCN structures with various single-atom metals, dopants, and nanoparticles for $CO_2$ reduction. Single-atom-impeded g-$C_3N_4$ for $CO_2$ reduction

is not studied enough. g-C$_3$N$_4$ comprises a triazine or heptazine skeleton that can accommodate various single-metal atoms to maximize atom utilization; minimize attrition; reduce deactivation; and enhance CO$_2$ activity, selectivity, and durability.

- Both experimental and theoretical calculations/simulations (i.e., DFT and artificial intelligence) could be coupled to understand the effect of non-metal dopants on the physicochemical properties of porous gCN nanostructures and their catalytic/photocatalytic activities and mechanisms.
- The relatively high overpotential, low current densities, and inferior long-term stability are critical barriers in gCNs for HERs, which cannot meet practical requirements (i.e., current density up to several ambers and durability for several weeks or months). This could be solved using noble metal dopants in the formation of heterojunction structures with porous metal oxynitride [165,166], multimetallic nanocrystals [12,167,168], MXenes [2,169–172], MOF [10,173,174], graphene [175], and graphdiyne [176] to augment solar light harvesting and charge carrier separation during the HER.
- The safety of H$_2$ storage tanks should be considered because in the case of unexpected accidents, the H$_2$ tank becomes a bomb. Defeating these barriers requires using high-pressure vessels made of fiber-based composites that can afford a high pressure of up to 700 bar and subsequently can improve cold or cryo-compressed hydrogen storage along with boosting H$_2$ density and using novel, durable, low-cost materials for H$_2$ adsorption [18,46–48]. Moreover, using novel adsorbents for H$_2$ storage is safer than tanks, but needs more efforts to decrease operation conditions (i.e., pressure) and enhance storage capacity.

**Author Contributions:** All authors contributed equally to this work. Data collection, methodology, and writing–original draft preparation (Q.L., A.A. and J.L.); conceptualization, revision and supervision and project administration (K.E.). All authors have read and agreed to the published version of the manuscript.

**Institutional Review Board Statement:** Not applicable.

**Informed Consent Statement:** Not applicable.

**Data Availability Statement:** The data presented in this study are available on request from the corresponding authors.

**Conflicts of Interest:** The authors declare no conflict of interest.

## References

1. Eid, K.; Sliem, M.H.; Al-Ejji, M.; Abdullah, A.M.; Harfouche, M.; Varma, R.S. Hierarchical Porous Carbon Nitride-Crumpled Nanosheet-Embedded Copper Single Atoms: An Efficient Catalyst for Carbon Monoxide Oxidation. *ACS Appl. Mater. Interfaces* **2022**, *14*, 40749–40760. [CrossRef]
2. Eid, K.; Lu, Q.; Abdel-Azeim, S.; Soliman, A.; Abdullah, A.M.; Abdelgwad, A.M.; Forbes, R.P.; Ozoemena, K.I.; Varma, R.S.; Shibl, M.F. Highly exfoliated Ti$_3$C$_2$T$_x$ MXene nanosheets atomically doped with Cu for efficient electrochemical CO$_2$ reduction: An experimental and theoretical study. *J. Mater. Chem. A* **2022**, *10*, 1965–1975. [CrossRef]
3. Eid, K.; Sliem, M.H.; Jlassi, K.; Eldesoky, A.S.; Abdo, G.G.; Al-Qaradawi, S.Y.; Sharaf, M.A.; Abdullah, A.M.; Elzatahry, A.A. Precise fabrication of porous one-dimensional gC$_3$N$_4$ nanotubes doped with Pd and Cu atoms for efficient CO oxidation and CO$_2$ reduction. *Inorg. Chem. Commun.* **2019**, *107*, 107460. [CrossRef]
4. Eid, K.; Sliem, M.H.; Al-Kandari, H.; Sharaf, M.A.; Abdullah, A.M. Rational synthesis of porous graphitic-like carbon nitride nanotubes codoped with Au and Pd as an efficient catalyst for carbon monoxide oxidation. *Langmuir* **2019**, *35*, 3421–3431. [CrossRef]

5.  Eid, K.; Sliem, M.H.; Eldesoky, A.S.; Al-Kandari, H.; Abdullah, A.M. Rational synthesis of one-dimensional carbon nitride-based nanofibers atomically doped with Au/Pd for efficient carbon monoxide oxidation. *Int. J. Hydrogen Energy* **2019**, *44*, 17943–17953. [CrossRef]
6.  Lu, Q.; Eid, K.; Li, W. Heteroatom-Doped Porous Carbon-Based Nanostructures for Electrochemical CO2 Reduction. *Nanomaterials* **2022**, *12*, 2379. [CrossRef]
7.  Abdu, H.I.; Eid, K.; Abdullah, A.M.; Sliem, M.H.; Elzatahry, A.; Lu, X. Dry ice-mediated rational synthesis of edge-carboxylated crumpled graphene nanosheets for selective and prompt hydrolysis of cellulose and eucalyptus lignocellulose under ambient reaction conditions. *Green Chem.* **2020**, *22*, 5437–5446. [CrossRef]
8.  Li, C.; Eid, K.; Wang, H.; Deng, Y.; Lu, S.; Li, X.; Wang, L.; Gu, H. One-pot synthesis of bimetallic PdCu nanoframes as an efficient catalyst for the methanol oxidation reaction. *New J. Chem.* **2018**, *42*, 798–801. [CrossRef]
9.  Lu, Q.; Li, J.; Eid, K.; Gu, X.; Wan, Z.; Li, W.; Al-Hajri, R.S.; Abdullah, A.M. Facile one-step aqueous-phase synthesis of porous PtBi nanosponges for efficient electrochemical methanol oxidation with a high CO tolerance. *J. Electroanal. Chem.* **2022**, *916*, 116361. [CrossRef]
10. Ahsan, M.A.; He, T.; Eid, K.; Abdullah, A.M.; Sanad, M.F.; Aldalbahi, A.; Alvarado-Tenorio, B.; Du, A.; Puente Santiago, A.R.; Noveron, J.C. Controlling the Interfacial Charge Polarization of MOF-Derived 0D–2D vdW Architectures as a Unique Strategy for Bifunctional Oxygen Electrocatalysis. *ACS Appl. Mater. Interfaces* **2022**, *14*, 3919–3929. [CrossRef]
11. Eid, K.; Ahmad, Y.H.; AlQaradawi, S.Y.; Allam, N.K. Rational design of porous binary Pt-based nanodendrites as efficient catalysts for direct glucose fuel cells over a wide pH range. *Catal. Sci. Technol.* **2017**, *7*, 2819–2827. [CrossRef]
12. Wang, H.; Yin, S.; Eid, K.; Li, Y.; Xu, Y.; Li, X.; Xue, H.; Wang, L. Fabrication of mesoporous cage-bell Pt nanoarchitectonics as efficient catalyst for oxygen reduction reaction. *ACS Sustain. Chem. Eng.* **2018**, *6*, 11768–11774. [CrossRef]
13. Zhang, H.; Wang, H.; Eid, K.; Wang, L. Nanoparticle in Nanocage: Au@ Porous Pt Yolk-Shell Nanoelectrocatalysts. *Part. Part. Syst. Charact.* **2015**, *32*, 863–868. [CrossRef]
14. Ahmed, A.; Al-Amin, A.Q.; Ambrose, A.F.; Saidur, R. Hydrogen fuel and transport system: A sustainable and environmental future. *Int. J. Hydrogen Energy* **2016**, *41*, 1369–1380. [CrossRef]
15. Manoharan, Y.; Hosseini, S.E.; Butler, B.; Alzhahrani, H.; Senior, B.T.F.; Ashuri, T.; Krohn, J. Hydrogen fuel cell vehicles; current status and future prospect. *Appl. Sci.* **2019**, *9*, 2296. [CrossRef]
16. Gamal, A.; Eid, K.; Abdullah, A.M. Engineering of Pt-based nanostructures for efficient dry ($CO_2$) reforming: Strategy and mechanism for rich-hydrogen production. *Int. J. Hydrogen Energy* **2021**, *47*, 5901–5928. [CrossRef]
17. Gamal, A.; Eid, K.; El-Naas, M.H.; Kumar, D.; Kumar, A. Catalytic methane decomposition to carbon nanostructures and $CO_x$-free hydrogen: A mini-review. *Nanomaterials* **2021**, *11*, 1226. [CrossRef]
18. Tarhan, C.; Çil, M.A. A study on hydrogen, the clean energy of the future: Hydrogen storage methods. *J. Energy Storage* **2021**, *40*, 102676. [CrossRef]
19. Olabi, A.; Abdelghafar, A.A.; Baroutaji, A.; Sayed, E.T.; Alami, A.H.; Rezk, H.; Abdelkareem, M.A. Large-vscale hydrogen production and storage technologies: Current status and future directions. *Int. J. Hydrogen Energy* **2021**, *46*, 23498–23528. [CrossRef]
20. Dawood, F.; Anda, M.; Shafiullah, G. Hydrogen production for energy: An overview. *Int. J. Hydrogen Energy* **2020**, *45*, 3847–3869.
21. Acar, C.; Dincer, I. Review and evaluation of hydrogen production options for better environment. *J. Clean. Prod.* **2019**, *218*, 835–849. [CrossRef]
22. Zhao, W.; Chen, Z.; Yang, X.; Qian, X.; Liu, C.; Zhou, D.; Sun, T.; Zhang, M.; Wei, G.; Dissanayake, P.D.; et al. Recent advances in photocatalytic hydrogen evolution with high-performance catalysts without precious metals. *Renew. Sustain. Energy Rev.* **2020**, *132*, 110040. [CrossRef]
23. Zhu, J.; Hu, L.; Zhao, P.; Lee, L.Y.S.; Wong, K.-Y. Recent Advances in Electrocatalytic Hydrogen Evolution Using Nanoparticles. *Chem. Rev.* **2020**, *120*, 851–918. [CrossRef] [PubMed]
24. Wan, D.; Yan, B.; Chen, J.; Wu, S.; Hong, J.; Song, D.; Zhao, X.; Chi, X.; Zeng, S.; Huang, Z.; et al. New Family of Plasmonic Photocatalysts without Noble Metals. *Chem. Mater.* **2019**, *31*, 2320–2327. [CrossRef]
25. Wu, H.; Feng, C.; Zhang, L.; Zhang, J.; Wilkinson, D.P. Non-noble Metal Electrocatalysts for the Hydrogen Evolution Reaction in Water Electrolysis. *Electrochem. Energy Rev.* **2021**, *4*, 473–507. [CrossRef]
26. Guo, J.; Zhou, J.; Sun, Z.; Wang, M.; Zou, X.; Mao, H.; Yan, F. Enhanced photocatalytic and antibacterial activity of acridinium-grafted g-$C_3N_4$ with broad-spectrum light absorption for antimicrobial photocatalytic therapy. *Acta Biomater.* **2022**, *146*, 370–384. [CrossRef]
27. Shi, L.; Liang, L.; Wang, F.; Ma, J.; Sun, J. Polycondensation of guanidine hydrochloride into a graphitic carbon nitride semiconductor with a large surface area as a visible light photocatalyst. *Catal. Sci. Technol.* **2014**, *4*, 3235–3243. [CrossRef]
28. Lu, Q.; Eid, K.; Li, W.; Abdullah, A.M.; Xu, G.; Varma, R.S. Engineering graphitic carbon nitride (gC$_3$N$_4$) for catalytic reduction of $CO_2$ to fuels and chemicals: Strategy and mechanism. *Green Chem.* **2021**, *23*, 5394–5428. [CrossRef]
29. Zhao, G.; Huang, X.; Wang, X.; Wang, X. Progress in catalyst exploration for heterogeneous CO2reduction and utilization: A critical review. *J. Mater. Chem. A* **2017**, *5*, 21625–21649. [CrossRef]
30. Wen, J.; Xie, J.; Chen, X.; Li, X. A review on g-$C_3N_4$-based photocatalysts. *Appl. Surf. Sci.* **2017**, *391*, 72–123. [CrossRef]

31. Ong, W.J.; Tan, L.L.; Ng, Y.H.; Yong, S.T.; Chai, S.P. Graphitic Carbon Nitride (g-C$_3$N$_4$)-Based Photocatalysts for Artificial Photosynthesis and Environmental Remediation: Are We a Step Closer To Achieving Sustainability? *Chem. Rev.* **2016**, *116*, 7159–7329. [CrossRef] [PubMed]

32. Wang, X.; Maeda, K.; Thomas, A.; Takanabe, K.; Xin, G.; Carlsson, J.M.; Domen, K.; Antonietti, M. A metal-free polymeric photocatalyst for hydrogen production from water under visible light. *Nat. Mater.* **2009**, *8*, 76–80. [CrossRef] [PubMed]

33. Zhang, H.; Liu, J.; Jiang, L. Photocatalytic hydrogen evolution based on carbon nitride and organic semiconductors. *Nanotechnology* **2022**, *33*, 322001. [CrossRef] [PubMed]

34. Dolai, S.; Bhunia, S.K.; Kluson, P.; Stavarek, P.; Pittermannova, A. Solvent-Assisted Synthesis of Supramolecular-Assembled Graphitic Carbon Nitride for Visible Light Induced Hydrogen Evolution–A Review. *ChemCatChem* **2022**, *14*, e202101299. [CrossRef]

35. Prasad, C.; Tang, H.; Liu, Q.; Bahadur, I.; Karlapudi, S.; Jiang, Y. A latest overview on photocatalytic application of g-C$_3$N$_4$ based nanostructured materials for hydrogen production. *Int. J. Hydrogen Energy* **2020**, *45*, 337–379. [CrossRef]

36. Rhimi, B.; Wang, C.; Bahnemann, D.W. Latest progress in g-C$_3$N$_4$ based heterojunctions for hydrogen production via photocatalytic water splitting: A mini review. *J. Phys. Energy* **2020**, *2*, 042003. [CrossRef]

37. Wang, T.; Tian, B.; Han, B.; Ma, D.; Sun, M.; Hanif, A.; Xia, D.; Shang, J. Recent advances on porous materials for synergetic adsorption and photocatalysis. *Energy Environ. Mater.* **2021**, *5*, 711–730. [CrossRef]

38. Su, K.; Deng, S.; Li, L.; Qin, Q.; Yang, J.; Chen, Y.; Zhang, S.; Chen, J. gC$_3$N$_4$ Derived Materials for Photocatalytic Hydrogen Production: A Mini Review on Design Strategies. *J. Renew. Mater.* **2022**, *10*, 653. [CrossRef]

39. Phoon, B.L.; Ong, C.C.; Lee, K.-C.; Pan, G.-T.; Leo, B.F.; Chong, S.; Pan, K.-L. Co-Doped, Tri-Doped, and Rare-Earth-Doped g-C$_3$N$_4$ for Photocatalytic Applications: State-of-the-Art. *Catalysts* **2022**, *12*, 586. [CrossRef]

40. Jin, H.; Liu, X.; Chen, S.; Vasileff, A.; Li, L.; Jiao, Y.; Song, L.; Zheng, Y.; Qiao, S.-Z. Heteroatom-doped transition metal electrocatalysts for hydrogen evolution reaction. *ACS Energy Lett.* **2019**, *4*, 805–810. [CrossRef]

41. Shcherban, N. Preparation, physicochemical properties, and functional characteristics of carbon nitride: A review. *Theor. Exp. Chem.* **2016**, *52*, 265–284. [CrossRef]

42. Wang, Y.; Liu, L.; Ma, T.; Zhang, Y.; Huang, H. 2D graphitic carbon nitride for energy conversion and storage. *Adv. Funct. Mater.* **2021**, *31*, 2102540. [CrossRef]

43. Hou, H.; Shao, G.; Yang, W. Recent advances in gC$_3$N$_4$-based photocatalysts incorporated by MXenes and their derivatives. *J. Mater. Chem. A* **2021**, *9*, 13722–13745. [CrossRef]

44. Abe, J.O.; Popoola, A.; Ajenifuja, E.; Popoola, O. Hydrogen energy, economy and storage: Review and recommendation. *Int. J. Hydrogen Energy* **2019**, *44*, 15072–15086. [CrossRef]

45. Zohuri, B. *Hydrogen Energy: Challenges and Solutions for a Cleaner Future*; Springer: Cham, Switzerland, 2019.

46. Rivard, E.; Trudeau, M.; Zaghib, K. Hydrogen storage for mobility: A review. *Materials* **2019**, *12*, 1973. [CrossRef]

47. Kaur, M.; Pal, K. Review on hydrogen storage materials and methods from an electrochemical viewpoint. *J. Energy Storage* **2019**, *23*, 234–249. [CrossRef]

48. Cousins, K.; Zhang, R. Highly porous organic polymers for hydrogen fuel storage. *Polymers* **2019**, *11*, 690. [CrossRef]

49. Zhao, D.; Weijie, Y.; Kaifu, H.; Leon, S. Thermodynamics and kinetics tuning of LiBH$_4$ for hydrogen storage. *Prog. Chem.* **2021**, *33*, 1586.

50. Ding, Z.; Li, S.; Zhou, Y.; Chen, Z.; Yang, W.; Ma, W.; Shaw, L. LiBH$_4$ for hydrogen storage-new perspectives. *Nano Mater. Sci.* **2020**, *2*, 109–119. [CrossRef]

51. Ding, Z.; Shaw, L. Enhancement of hydrogen desorption from nanocomposite prepared by ball milling MgH$_2$ with in situ aerosol spraying LiBH$_4$. *ACS Sustain. Chem. Eng.* **2019**, *7*, 15064–15072. [CrossRef]

52. Ding, Z.; Lu, Y.; Li, L.; Shaw, L. High reversible capacity hydrogen storage through Nano-LiBH$_4$+ Nano-MgH$_2$ system. *Energy Storage Mater.* **2019**, *20*, 24–35. [CrossRef]

53. Ding, Z.; Wu, P.; Shaw, L. Solid-state hydrogen desorption of 2 MgH$_2$+ LiBH$_4$ nano-mixture: A kinetics mechanism study. *J. Alloys Compd.* **2019**, *806*, 350–360. [CrossRef]

54. Ding, Z.; Chen, Z.; Ma, T.; Lu, C.-T.; Ma, W.; Shaw, L. Predicting the hydrogen release ability of LiBH$_4$-based mixtures by ensemble machine learning. *Energy Storage Mater.* **2020**, *27*, 466–477. [CrossRef]

55. Ding, Z.; Zhao, X.; Shaw, L.L. Reaction between LiBH$_4$ and MgH$_2$ induced by high-energy ball milling. *J. Power Sources* **2015**, *293*, 236–245. [CrossRef]

56. Ding, Z.; Li, H.; Shaw, L. New insights into the solid-state hydrogen storage of nanostructured LiBH$_4$-MgH$_2$ system. *Chem. Eng. J.* **2020**, *385*, 123856. [CrossRef]

57. Chen, Z.; Keene, S.; Gaieck, W.; Phun, G.S.; Stinson, R.; Stinson, W.D.; Wang, Y.; Barrera, L.; Chen, Z.; Mayer, M. Optimization of Z-Scheme Photocatalytic Reactors for Solar Water Splitting. In *ECS Meeting Abstracts*; IOP Publishing: Bristol, UK, 2022; p. 1553.

58. Pivovar, B.S.; Ruth, M.F.; Myers, D.J.; Dinh, H.N. Hydrogen: Targeting $1/kg in 1 Decade. *Electrochem. Soc. Interface* **2021**, *30*, 61. [CrossRef]

59. Scheffe, J.R.; Haussener, S.; Patzke, G.R. Solar Hydrogen Production. *Energy Technol.* **2022**, *10*, 2101021. [CrossRef]

60. Jiang, L.; Yuan, X.; Pan, Y.; Liang, J.; Zeng, G.; Wu, Z.; Wang, H. Doping of graphitic carbon nitride for photocatalysis: A reveiw. *Appl. Catal. B Environ.* **2017**, *217*, 388–406. [CrossRef]

61. Xiao, N.; Li, S.; Li, X.; Ge, L.; Gao, Y.; Li, N. The roles and mechanism of cocatalysts in photocatalytic water splitting to produce hydrogen. *Chin. J. Catal.* **2020**, *41*, 642–671. [CrossRef]

62. McCrory, C.C.; Jung, S.; Peters, J.C.; Jaramillo, T.F. Benchmarking heterogeneous electrocatalysts for the oxygen evolution reaction. *J. Am. Chem. Soc.* **2013**, *135*, 16977–16987. [CrossRef]

63. Liu, Y.; Hu, M.; Xu, W.; Wu, X.; Jiang, J. Catalytically active carbon from cattail fibers for electrochemical reduction reaction. *Front. Chem.* **2019**, *7*, 786. [CrossRef] [PubMed]

64. Zhu, J.; Xiao, P.; Li, H.; Carabineiro, S.A. Graphitic carbon nitride: Synthesis, properties, and applications in catalysis. *ACS Appl. Mater. Interfaces* **2014**, *6*, 16449–16465. [CrossRef] [PubMed]

65. Liang, Q.; Li, Z.; Huang, Z.H.; Kang, F.; Yang, Q.H. Holey graphitic carbon nitride nanosheets with carbon vacancies for highly improved photocatalytic hydrogen production. *Adv. Funct. Mater.* **2015**, *25*, 6885–6892. [CrossRef]

66. Wang, Y.; Wang, X.; Antonietti, M. Polymeric Graphitic Carbon Nitride as a Heterogeneous Organocatalyst: From Photochemistry to Multipurpose Catalysis to Sustainable Chemistry. *Angew. Chem. Int. Ed.* **2012**, *51*, 68–89. [CrossRef] [PubMed]

67. Gao, J.; Zhou, Y.; Li, Z.; Yan, S.; Wang, N.; Zou, Z. High-yield synthesis of millimetre-long, semiconducting carbon nitride nanotubes with intense photoluminescence emission and reproducible photoconductivity. *Nanoscale* **2012**, *4*, 3687–3692. [CrossRef]

68. Ding, F.; Yang, D.; Tong, Z.; Nan, Y.; Wang, Y.; Zou, X.; Jiang, Z. Graphitic carbon nitride-based nanocomposites as visible-light driven photocatalysts for environmental purification. *Environ. Sci. Nano* **2017**, *4*, 1455–1469. [CrossRef]

69. Lai, J.; Li, S.; Wu, F.; Saqib, M.; Luque, R.; Xu, G. Unprecedented metal-free 3D porous carbonaceous electrodes for full water splitting. *Energy Environ. Sci.* **2016**, *9*, 1210–1214. [CrossRef]

70. Zhao, J.; Gilani, M.R.H.S.; Liu, Z.; Luque, R.; Xu, G. Facile surfactant-free synthesis of polybenzoxazine-based polymer and nitrogen-doped carbon nanospheres. *Polym. Chem.* **2018**, *9*, 4324–4331. [CrossRef]

71. Wei, D.; Liu, Y.; Wang, Y.; Zhang, H.; Huang, L.; Yu, G. Synthesis of N-doped graphene by chemical vapor deposition and its electrical properties. *Nano Lett.* **2009**, *9*, 1752–1758. [CrossRef]

72. Li, X.; Fan, L.; Li, Z.; Wang, K.; Zhong, M.; Wei, J.; Wu, D.; Zhu, H. Boron doping of graphene for graphene–silicon p–n junction solar cells. *Adv. Energy Mater.* **2012**, *2*, 425–429. [CrossRef]

73. Zhao, C.; Chen, Z.; Xu, J.; Liu, Q.; Xu, H.; Tang, H.; Li, G.; Jiang, Y.; Qu, F.; Lin, Z. Probing supramolecular assembly and charge carrier dynamics toward enhanced photocatalytic hydrogen evolution in 2D graphitic carbon nitride nanosheets. *Appl. Catal. B Environ.* **2019**, *256*, 117867. [CrossRef]

74. Wang, Y.; Liu, X.; Liu, J.; Han, B.; Hu, X.; Yang, F.; Xu, Z.; Li, Y.; Jia, S.; Li, Z. Carbon quantum dot implanted graphite carbon nitride nanotubes: Excellent charge separation and enhanced photocatalytic hydrogen evolution. *Angew. Chem.* **2018**, *130*, 5867–5873. [CrossRef]

75. Huo, T.; Ba, G.; Deng, Q.; Yu, F.; Wang, G.; Li, H.; Hou, W. A dual strategy for synthesizing carbon/defect comodified polymeric carbon nitride porous nanotubes with boosted photocatalytic hydrogen evolution and synchronous contaminant degradation. *Appl. Catal. B Environ.* **2021**, *287*, 119995. [CrossRef]

76. Zhu, Y.-P.; Ren, T.-Z.; Yuan, Z.-Y. Mesoporous phosphorus-doped g-C$_3$N$_4$ nanostructured flowers with superior photocatalytic hydrogen evolution performance. *ACS Appl. Mater. Interfaces* **2015**, *7*, 16850–16856. [CrossRef]

77. Zhou, L.; Zhang, H.; Sun, H.; Liu, S.; Tade, M.O.; Wang, S.; Jin, W. Recent advances in non-metal modification of graphitic carbon nitride for photocatalysis: A historic review. *Catal. Sci. Technol.* **2016**, *6*, 7002–7023. [CrossRef]

78. Mun, S.J.; Park, S.-J. Graphitic carbon nitride materials for photocatalytic hydrogen production via water splitting: A short review. *Catalysts* **2019**, *9*, 805. [CrossRef]

79. Naseri, A.; Samadi, M.; Pourjavadi, A.; Moshfegh, A.Z.; Ramakrishna, S. Graphitic carbon nitride (gC$_3$N$_4$)-based photocatalysts for solar hydrogen generation: Recent advances and future development directions. *J. Mater. Chem. A* **2017**, *5*, 23406–23433. [CrossRef]

80. Jiang, H.; Li, Y.; Wang, D.; Hong, X.; Liang, B. Recent advances in heteroatom doped graphitic carbon nitride (g-C$_3$N$_4$) and g-C$_3$N$_4$/metal oxide composite photocatalysts. *Curr. Org. Chem.* **2020**, *24*, 673–693. [CrossRef]

81. Ye, L.; Wang, D.; Chen, S. Fabrication and enhanced photoelectrochemical performance of MoS2/S-doped g-C$_3$N$_4$ heterojunction film. *ACS Appl. Mater. Interfaces* **2016**, *8*, 5280–5289. [CrossRef]

82. Wang, J.; Han, W.Q. A review of heteroatom doped materials for advanced lithium–sulfur batteries. *Adv. Funct. Mater.* **2022**, *32*, 2107166. [CrossRef]

83. Zhang, H.; Tian, W.; Duan, X.; Sun, H.; Shen, Y.; Shao, G.; Wang, S. Functional carbon nitride materials for water oxidation: From heteroatom doping to interface engineering. *Nanoscale* **2020**, *12*, 6937–6952. [CrossRef] [PubMed]

84. Zhang, D.; He, W.; Ye, J.; Gao, X.; Wang, D.; Song, J. Polymeric Carbon Nitride-Derived Photocatalysts for Water Splitting and Nitrogen Fixation. *Small* **2021**, *17*, 2005149. [CrossRef]

85. Belgacem, A.B.; Hinkov, I.; Yahia, S.B.; Brinza, O.; Farhat, S. Arc discharge boron nitrogen doping of carbon nanotubes. *Mater. Today Commun.* **2016**, *8*, 183–195. [CrossRef]

86. Ma, L.; Hu, S.; Li, P.; Wang, Q.; Ma, H.; Li, W. In situ synthesis of sulfur doped carbon nitride with enhanced photocatalytic performance using DBD plasma treatment under H$_2$S atmosphere. *J. Phys. Chem. Solids* **2018**, *118*, 166–171. [CrossRef]

87. Zhang, J.; Chen, Y.; Wang, X. Two-dimensional covalent carbon nitride nanosheets: Synthesis, functionalization, and applications. *Energy Environ. Sci.* **2015**, *8*, 3092–3108. [CrossRef]

88. Han, Q.; Hu, C.; Zhao, F.; Zhang, Z.; Chen, N.; Qu, L. One-step preparation of iodine-doped graphitic carbon nitride nanosheets as efficient photocatalysts for visible light water splitting. *J. Mater. Chem. A* **2015**, *3*, 4612–4619. [CrossRef]

89. Ran, J.; Ma, T.Y.; Gao, G.; Du, X.-W.; Qiao, S.Z. Porous P-doped graphitic carbon nitride nanosheets for synergistically enhanced visible-light photocatalytic H$_2$ production. *Energy Environ. Sci.* **2015**, *8*, 3708–3717. [CrossRef]

90. Zhou, Y.; Zhang, L.; Liu, J.; Fan, X.; Wang, B.; Wang, M.; Ren, W.; Wang, J.; Li, M.; Shi, J. Brand new P-doped gC$_3$N$_4$: Enhanced photocatalytic activity for H$_2$ evolution and Rhodamine B degradation under visible light. *J. Mater. Chem. A* **2015**, *3*, 3862–3867. [CrossRef]

91. Guo, S.; Deng, Z.; Li, M.; Jiang, B.; Tian, C.; Pan, Q.; Fu, H. Phosphorus-doped carbon nitride tubes with a layered micro-nanostructure for enhanced visible-light photocatalytic hydrogen evolution. *Angew. Chem.* **2016**, *128*, 1862–1866. [CrossRef]

92. Guo, S.; Tang, Y.; Xie, Y.; Tian, C.; Feng, Q.; Zhou, W.; Jiang, B. P-doped tubular g-C$_3$N$_4$ with surface carbon defects: Universal synthesis and enhanced visible-light photocatalytic hydrogen production. *Appl. Catal. B Environ.* **2017**, *218*, 664–671. [CrossRef]

93. Zhang, L.; Zhang, Y.; Shi, R.; Bao, S.; Wang, J.; Amini, A.; Chandrashekar, B.N.; Cheng, C. Phosphorous doped graphitic-C$_3$N$_4$ hierarchical architecture for hydrogen production from water under visible light. *Mater. Today Energy* **2017**, *5*, 91–98. [CrossRef]

94. Cao, S.; Huang, Q.; Zhu, B.; Yu, J. Trace-level phosphorus and sodium co-doping of g-C$_3$N$_4$ for enhanced photocatalytic H$_2$ production. *J. Power Sources* **2017**, *351*, 151–159. [CrossRef]

95. Fang, H.-B.; Zhang, X.-H.; Wu, J.; Li, N.; Zheng, Y.-Z.; Tao, X. Fragmented phosphorus-doped graphitic carbon nitride nanoflakes with broad sub-bandgap absorption for highly efficient visible-light photocatalytic hydrogen evolution. *Appl. Catal. B Environ.* **2018**, *225*, 397–405. [CrossRef]

96. Wu, M.; Zhang, J.; He, B.-b.; Wang, H.-w.; Wang, R.; Gong, Y.-s. In-situ construction of coral-like porous P-doped g-C$_3$N$_4$ tubes with hybrid 1D/2D architecture and high efficient photocatalytic hydrogen evolution. *Appl. Catal. B Environ.* **2019**, *241*, 159–166. [CrossRef]

97. Yang, H.; Zhou, Y.; Wang, Y.; Hu, S.; Wang, B.; Liao, Q.; Li, H.; Bao, J.; Ge, G.; Jia, S. Three-dimensional flower-like phosphorus-doped gC$_3$N$_4$ with a high surface area for visible-light photocatalytic hydrogen evolution. *J. Mater. Chem. A* **2018**, *6*, 16485–16494. [CrossRef]

98. Sun, Y.-j.; He, J.-y.; Zhang, D.; Wang, X.-j.; Zhao, J.; Liu, R.-h.; Li, F.-t. Simultaneous construction of dual-site phosphorus modified g-C$_3$N$_4$ and its synergistic mechanism for enhanced visible-light photocatalytic hydrogen evolution. *Appl. Surf. Sci.* **2020**, *517*, 146192. [CrossRef]

99. Zhu, Y.; Li, J.; Cao, J.; Lv, C.; Huang, G.; Zhang, G.; Xu, Y.; Zhang, S.; Meng, P.; Zhan, T. Phosphorus-doped polymeric carbon nitride nanosheets for enhanced photocatalytic hydrogen production. *APL Mater.* **2020**, *8*, 041108. [CrossRef]

100. Yu, D.; Jia, T.; Deng, Z.; Wei, Q.; Wang, K.; Chen, L.; Wang, P.; Cui, J. One-Dimensional P-Doped Graphitic Carbon Nitride Tube: Facile Synthesis, Effect of Doping Concentration, and Enhanced Mechanism for Photocatalytic Hydrogen Evolution. *Nanomaterials* **2022**, *12*, 1759. [CrossRef]

101. Li, B.; Si, Y.; Fang, Q.; Shi, Y.; Huang, W.-Q.; Hu, W.; Pan, A.; Fan, X.; Huang, G.-F. Hierarchical self-assembly of well-defined Louver-like P-doped carbon nitride nanowire arrays with highly efficient hydrogen evolution. *Nano-Micro Lett.* **2020**, *12*, 1–16. [CrossRef]

102. Zhang, F.; Li, J.; Wang, H.; Li, Y.; Liu, Y.; Qian, Q.; Jin, X.; Wang, X.; Zhang, J.; Zhang, G. Realizing synergistic effect of electronic modulation and nanostructure engineering over graphitic carbon nitride for highly efficient visible-light H$_2$ production coupled with benzyl alcohol oxidation. *Appl. Catal. B Environ.* **2020**, *269*, 118772. [CrossRef]

103. Zhan, X.; Zhao, Y.; Zhou, G.; Yu, J.; Wang, H.; Shi, H. Oxygen-containing groups and P doped porous carbon nitride nanosheets towards enhanced photocatalytic activity. *Chemosphere* **2022**, *287*, 132399. [CrossRef] [PubMed]

104. Sun, C.; Zhang, H.; Liu, H.; Zheng, X.; Zou, W.; Dong, L.; Qi, L. Enhanced activity of visible-light photocatalytic H$_2$ evolution of sulfur-doped g-C$_3$N$_4$ photocatalyst via nanoparticle metal Ni as cocatalyst. *Appl. Catal. B Environ.* **2018**, *235*, 66–74. [CrossRef]

105. Wang, H.; Bian, Y.; Hu, J.; Dai, L. Highly crystalline sulfur-doped carbon nitride as photocatalyst for efficient visible-light hydrogen generation. *Appl. Catal. B Environ.* **2018**, *238*, 592–598. [CrossRef]

106. Zhou, Y.; Lv, W.; Zhu, B.; Tong, F.; Pan, J.; Bai, J.; Zhou, Q.; Qin, H. Template-free one-step synthesis of g-C$_3$N$_4$ nanosheets with simultaneous porous network and S-doping for remarkable visible-light-driven hydrogen evolution. *ACS Sustain. Chem. Eng.* **2019**, *7*, 5801–5807. [CrossRef]

107. Bi, J.; Zhu, L.; Wu, J.; Xu, Y.; Wang, Z.; Zhang, X.; Han, Y. Optimizing electronic structure and charge transport of sulfur/potassium co-doped graphitic carbon nitride with efficient photocatalytic hydrogen evolution performance. *Appl. Organomet. Chem.* **2019**, *33*, e5163. [CrossRef]

108. Lv, H.; Huang, Y.; Koodali, R.T.; Liu, G.; Zeng, Y.; Meng, Q.; Yuan, M. Synthesis of sulfur-doped 2D graphitic carbon nitride nanosheets for efficient photocatalytic degradation of phenol and hydrogen evolution. *ACS Appl. Mater. Interfaces* **2020**, *12*, 12656–12667. [CrossRef]

109. Zhang, X.; Yang, C.; Xue, Z.; Zhang, C.; Qin, J.; Liu, R. Spatial separation of charge carriers via heterogeneous structural defects in graphitic carbon nitride for photocatalytic hydrogen evolution. *ACS Appl. Nano Mater.* **2020**, *3*, 4428–4436. [CrossRef]

110. Luo, L.; Gong, Z.; Ma, J.; Wang, K.; Zhu, H.; Li, K.; Xiong, L.; Guo, X.; Tang, J. Ultrathin sulfur-doped holey carbon nitride nanosheets with superior photocatalytic hydrogen production from water. *Appl. Catal. B Environ.* **2021**, *284*, 119742. [CrossRef]

111. Bai, J.; Zhou, P.; Xu, P.; Deng, Y.; Zhou, Q. Synergy of dopants and porous structures in graphitic carbon nitride for efficient photocatalytic H$_2$ evolution. *Ceram. Int.* **2021**, *47*, 4043–4048. [CrossRef]

112. Fei, T.; Qin, C.; Zhang, Y.; Dong, G.; Wang, Y.; Zhou, Y.; Cui, M. A 3D peony-like sulfur-doped carbon nitride synthesized by self-assembly for efficient photocatalytic hydrogen production. *Int. J. Hydrogen Energy* **2021**, *46*, 20481–20491. [CrossRef]

113. Hong, J.; Xia, X.; Wang, Y.; Xu, R. Mesoporous carbon nitride with in situ sulfur doping for enhanced photocatalytic hydrogen evolution from water under visible light. *J. Mater. Chem.* **2012**, *22*, 15006–15012. [CrossRef]

114. Feng, L.-L.; Zou, Y.; Li, C.; Gao, S.; Zhou, L.-J.; Sun, Q.; Fan, M.; Wang, H.; Wang, D.; Li, G.-D. Nanoporous sulfur-doped graphitic carbon nitride microrods: A durable catalyst for visible-light-driven H$_2$ evolution. *Int. J. Hydrogen Energy* **2014**, *39*, 15373–15379. [CrossRef]

115. Gu, Q.; Liu, J.; Gao, Z.; Xue, C. Homogenous boron-doping in self-sensitized carbon nitride for enhanced visible-light photocatalytic activity. *Chem.—Asian J.* **2016**, *11*, 3169–3173. [CrossRef]

116. Xing, W.; Chen, G.; Li, C.; Han, Z.; Hu, Y.; Meng, Q. Doping effect of non-metal group in porous ultrathin gC$_3$N$_4$ nanosheets towards synergistically improved photocatalytic hydrogen evolution. *Nanoscale* **2018**, *10*, 5239–5245. [CrossRef]

117. Bao, H.; Wang, L.; Li, G.; Zhou, L.; Xu, Y.; Liu, Z.; Wu, M. Carrier engineering of carbon nitride boosts visible-light photocatalytic hydrogen evolution. *Carbon* **2021**, *179*, 80–88. [CrossRef]

118. Mahvelati-Shamsabadi, T.; Fattahimoghaddam, H.; Lee, B.-K.; Ryu, H.; Jang, J. Caesium sites coordinated in Boron-doped porous and wrinkled graphitic carbon nitride nanosheets for efficient charge carrier separation and Transfer: Photocatalytic H$_2$ and H$_2$O$_2$ production. *Chem. Eng. J.* **2021**, *423*, 130067. [CrossRef]

119. Qi, K.; Cui, N.; Zhang, M.; Ma, Y.; Wang, G.; Zhao, Z.; Khataee, A. Ionic liquid-assisted synthesis of porous boron-doped graphitic carbon nitride for photocatalytic hydrogen production. *Chemosphere* **2021**, *272*, 129953. [CrossRef] [PubMed]

120. Chi, X.; Liu, F.; Gao, Y.; Song, J.; Guan, R.; Yuan, H. An efficient B/Na co-doped porous g-C$_3$N$_4$ nanosheets photocatalyst with enhanced photocatalytic hydrogen evolution and degradation of tetracycline under visible light. *Appl. Surf. Sci.* **2022**, *576*, 151837. [CrossRef]

121. Chen, L.; Wang, Y.; Cheng, S.; Zhao, X.; Zhang, J.; Ao, Z.; Zhao, C.; Li, B.; Wang, S.; Wang, S. Nitrogen defects/boron dopants engineered tubular carbon nitride for efficient tetracycline hydrochloride photodegradation and hydrogen evolution. *Appl. Catal. B Environ.* **2022**, *303*, 120932. [CrossRef]

122. Li, J.; Shen, B.; Hong, Z.; Lin, B.; Gao, B.; Chen, Y. A facile approach to synthesize novel oxygen-doped g-C$_3$N$_4$ with superior visible-light photoreactivity. *Chem. Commun.* **2012**, *48*, 12017–12019. [CrossRef]

123. Huang, Z.-F.; Song, J.; Pan, L.; Wang, Z.; Zhang, X.; Zou, J.-J.; Mi, W.; Zhang, X.; Wang, L. Carbon nitride with simultaneous porous network and O-doping for efficient solar-energy-driven hydrogen evolution. *Nano Energy* **2015**, *12*, 646–656. [CrossRef]

124. Guo, S.; Zhu, Y.; Yan, Y.; Min, Y.; Fan, J.; Xu, Q. Holey structured graphitic carbon nitride thin sheets with edge oxygen doping via photo-Fenton reaction with enhanced photocatalytic activity. *Appl. Catal. B Environ.* **2016**, *185*, 315–321. [CrossRef]

125. Wang, C.; Fan, H.; Ren, X.; Ma, J.; Fang, J.; Wang, W. Hydrothermally induced O-doping and porous structure of graphitic carbon nitride with highly ordered architecture and dramatically enhanced photocatalytic property. *ChemSusChem* **2018**, *11*, 700–708. [CrossRef] [PubMed]

126. Zhang, J.-W.; Gong, S.; Mahmood, N.; Pan, L.; Zhang, X.; Zou, J.-J. Oxygen-doped nanoporous carbon nitride via water-based homogeneous supramolecular assembly for photocatalytic hydrogen evolution. *Appl. Catal. B Environ.* **2018**, *221*, 9–16. [CrossRef]

127. Jiang, Y.; Sun, Z.; Tang, C.; Zhou, Y.; Zeng, L.; Huang, L. Enhancement of photocatalytic hydrogen evolution activity of porous oxygen doped g-C$_3$N$_4$ with nitrogen defects induced by changing electron transition. *Appl. Catal. B Environ.* **2019**, *240*, 30–38. [CrossRef]

128. Song, P.; Liang, S.; Cui, J.; Ren, D.; Duan, R.; Yang, Q.; Sun, S. Purposefully designing novel hydroxylated and carbonylated melamine towards the synthesis of targeted porous oxygen-doped gC$_3$N$_4$ nanosheets for highly enhanced photocatalytic hydrogen production. *Catal. Sci. Technol.* **2019**, *9*, 5150–5159. [CrossRef]

129. Huang, J.; Wang, H.; Yu, H.; Zhang, Q.; Cao, Y.; Peng, F. Oxygen doping in graphitic carbon nitride for enhanced photocatalytic hydrogen evolution. *ChemSusChem* **2020**, *13*, 5041–5049. [CrossRef]

130. Wei, H.; Zhang, Y.; Zhang, G.; Cui, J.; Wang, Y.; Qin, Y.; Zhang, X.; Tan, H.H.; Liu, J.; Wu, Y. In situ W/O Co-doped hollow carbon nitride tubular structures with enhanced visible-light-driven photocatalytic performance for hydrogen evolution. *Int. J. Hydrogen Energy* **2021**, *46*, 234–246. [CrossRef]

131. Wang, X.; Zhao, Y.; Tan, H.; Sun, H.; Shang, Q.; Zhao, X.; Qiu, T.; Li, Y. Foamer-derived bulk nitrogen defects and oxygen-doped porous carbon nitride with greatly extended visible-light response and efficient photocatalytic activity. *ACS Appl. Mater. Interfaces* **2021**, *13*, 23866–23876. [CrossRef]

132. Wu, Y.; Xiong, P.; Wu, J.; Huang, Z.; Sun, J.; Liu, Q.; Cheng, X.; Yang, J.; Zhu, J.; Zhou, Y. Band engineering and morphology control of oxygen-incorporated graphitic carbon nitride porous nanosheets for highly efficient photocatalytic hydrogen evolution. *Nano-Micro Lett.* **2021**, *13*, 48. [CrossRef]

133. Wen, J.; Zhang, S.; Liu, Y.; Zhai, Y. Formic acid assisted Fabrication of Oxygen-doped Rod-like Carbon Nitride with Improved Photocatalytic Hydrogen Evolution. *J. Colloid Interface Sci.* **2022**, *624*, 338–347. [CrossRef]

134. Song, T.; Hou, L.; Long, B.; Ali, A.; Deng, G.-J. Constructing ultralong hollow chain-ball-like carbon nitride implanted with oxygen for superior visible-light photocatalytic hydrogen production. *J. Alloys Compd.* **2021**, *857*, 157609. [CrossRef]

135. Li, J.; Wu, D.; Iocozzia, J.; Du, H.; Liu, X.; Yuan, Y.; Zhou, W.; Li, Z.; Xue, Z.; Lin, Z. Achieving efficient incorporation of Π-electrons into graphitic carbon nitride for markedly improved hydrogen generation. *Angew. Chem.* **2019**, *131*, 2007–2011. [CrossRef] [PubMed]

136. Chen, Z.; Fan, T.-T.; Yu, X.; Wu, Q.-L.; Zhu, Q.-H.; Zhang, L.-Z.; Li, J.-H.; Fang, W.-P.; Yi, X.-D. Gradual carbon doping of graphitic carbon nitride towards metal-free visible light photocatalytic hydrogen evolution. *J. Mater. Chem. A* **2018**, *6*, 15310–15319. [CrossRef]

137. Jiang, Y.; Lin, Z.; Zhang, Y.; Lai, Y.; Liang, D.; Yang, C. Facile synthesis of porous C-doped $C_3N_4$: Fast charge separation and enhanced photocatalytic hydrogen evolution. *New J. Chem.* **2020**, *44*, 17891–17898. [CrossRef]

138. Li, Q.; Zhang, L.; Liu, J.; Zhou, J.; Jiao, Y.; Xiao, X.; Zhao, C.; Zhou, Y.; Ye, S.; Jiang, B. Porous Carbon Nitride Thin Strip: Precise Carbon Doping Regulating Delocalized π-Electron Induces Elevated Photocatalytic Hydrogen Evolution. *Small* **2021**, *17*, 2006622. [CrossRef]

139. Liu, Y.; Zhao, S.; Zhang, C.; Fang, J.; Xie, L.; Zhou, Y.; Zhuo, S. Hollow tubular carbon doping graphitic carbon nitride with adjustable structure for highly enhanced photocatalytic hydrogen production. *Carbon* **2021**, *182*, 287–296. [CrossRef]

140. Fang, J.; Fan, H.; Li, M.; Long, C. Nitrogen self-doped graphitic carbon nitride as efficient visible light photocatalyst for hydrogen evolution. *J. Mater. Chem. A* **2015**, *3*, 13819–13826. [CrossRef]

141. Xu, F.; Mo, Z.; Yan, J.; Fu, J.; Song, Y.; El-Alami, W.; Wu, X.; Li, H.; Xu, H. Nitrogen-rich graphitic carbon nitride nanotubes for photocatalytic hydrogen evolution with simultaneous contaminant degradation. *J. Colloid Interface Sci.* **2020**, *560*, 555–564. [CrossRef]

142. Guo, F.; Wang, L.; Sun, H.; Li, M.; Shi, W. High-efficiency photocatalytic water splitting by a N-doped porous $gC_3N_4$ nanosheet polymer photocatalyst derived from urea and N, N-dimethylformamide. *Inorg. Chem. Front.* **2020**, *7*, 1770–1779. [CrossRef]

143. Liang, L.; Cong, Y.; Yao, L.; Wang, F.; Shi, L. One step to prepare Cl doped porous defect modified g-$C_3N_4$ with improved visible-light photocatalytic performance for $H_2$ production and rhodamine B degradation. *Mater. Res. Express* **2018**, *5*, 115510. [CrossRef]

144. Peng, X.; Li, J.; Liu, X.; Yi, L.; Cai, P.; Wen, Z. Cl-doped carbon nitride nanostrips for remarkably improving visible-light photocatalytic hydrogen production. *Int. J. Hydrogen Energy* **2021**, *46*, 28591–28601. [CrossRef]

145. Gao, Y.; Hou, F.; Hu, S.; Wu, B.; Jiang, B. Synchronization iodine surface modification and lattice doping porous carbon nitride for photocatalytic hydrogen production. *Appl. Surf. Sci.* **2019**, *481*, 1089–1095. [CrossRef]

146. Lan, Z.-A.; Zhang, G.; Wang, X. A facile synthesis of Br-modified g-$C_3N_4$ semiconductors for photoredox water splitting. *Appl. Catal. B Environ.* **2016**, *192*, 116–125. [CrossRef]

147. Hu, S.; Ma, L.; You, J.; Li, F.; Fan, Z.; Lu, G.; Liu, D.; Gui, J. Enhanced visible light photocatalytic performance of g-$C_3N_4$ photocatalysts co-doped with iron and phosphorus. *Appl. Surf. Sci.* **2014**, *311*, 164–171. [CrossRef]

148. Fan, Q.; Liu, J.; Yu, Y.; Zuo, S.; Li, B. A simple fabrication for sulfur doped graphitic carbon nitride porous rods with excellent photocatalytic activity degrading RhB dye. *Appl. Surf. Sci.* **2017**, *391*, 360–368. [CrossRef]

149. Wang, H.; Yang, C.; Li, M.; Chen, F.; Cui, Y. Enhanced photocatalytic hydrogen production of restructured B/F codoped g-$C_3N_4$ via post-thermal treatment. *Mater. Lett.* **2018**, *212*, 319–322. [CrossRef]

150. Cui, Y.; Wang, H.; Yang, C.; Li, M.; Zhao, Y.; Chen, F. Post-activation of in situ BF codoped g-$C_3N_4$ for enhanced photocatalytic $H_2$ evolution. *Appl. Surf. Sci.* **2018**, *441*, 621–630. [CrossRef]

151. Du, J.; Li, S.; Du, Z.; Meng, S.; Li, B. Boron/oxygen-codoped graphitic carbon nitride nanomesh for efficient photocatalytic hydrogen evolution. *Chem. Eng. J.* **2021**, *407*, 127114. [CrossRef]

152. Babu, P.; Mohanty, S.; Naik, B.; Parida, K. Synergistic effects of boron and sulfur Co-doping into graphitic carbon nitride framework for enhanced photocatalytic activity in visible light driven hydrogen generation. *ACS Appl. Energy Mater.* **2018**, *1*, 5936–5947. [CrossRef]

153. Yang, C.; Teng, W.; Song, Y.; Cui, Y. CI codoped porous g-$C_3N_4$ for superior photocatalytic hydrogen evolution. *Chin. J. Catal.* **2018**, *39*, 1615–1624. [CrossRef]

154. Wang, H.; Wang, B.; Bian, Y.; Dai, L. Enhancing photocatalytic activity of graphitic carbon nitride by codoping with P and C for efficient hydrogen generation. *ACS Appl. Mater. Interfaces* **2017**, *9*, 21730–21737. [CrossRef] [PubMed]

155. Zhou, P.; Meng, X.; Li, L.; Sun, T. P, S Co-doped g-$C_3N_4$ isotype heterojunction composites for high-efficiency photocatalytic H2 evolution. *J. Alloys Compd.* **2020**, *827*, 154259. [CrossRef]

156. Liu, K.; Ma, J.; Yang, X.; Liu, Z.; Li, X.; Zhang, J.; Cui, R.; Sun, R. Phosphorus/oxygen co-doping in hollow-tube-shaped carbon nitride for efficient simultaneous visible-light-driven water splitting and biorefinery. *Chem. Eng. J.* **2022**, *437*, 135232. [CrossRef]

157. Jiang, Y.; Fang, S.; Cao, C.; Hong, E.; Zeng, L.; Yang, W.; Huang, L.; Yang, C. Enhanced light harvesting and charge separation of carbon and oxygen co-doped carbon nitride as excellent photocatalyst for hydrogen evolution reaction. *J. Colloid Interface Sci.* **2022**, *612*, 367–376. [CrossRef] [PubMed]

158. Wang, B.; Bai, C.; Wang, Z.; She, P.; Sun, H.; Lu, G.; Liang, S.; Liu, Z. Phosphorus–Oxygen-Codoped Graphitic Carbon Nitride for Enhanced Hydrogen Evolution and Photocatalytic Degradation under Visible Light Irradiation. *ACS Appl. Energy Mater.* **2022**, *5*, 5774–5784. [CrossRef]

159. Jiao, Y.; Liu, M.; Qin, J.; Li, Y.; Wang, J.; He, Z.; Li, Z. Sulfur/phosphorus doping-mediated morphology transformation of carbon nitride from rods to porous microtubes with superior photocatalytic activity. *J. Colloid Interface Sci.* **2022**, *608*, 1432–1440. [CrossRef]

160. Li, J.; Qi, Y.; Mei, Y.; Ma, S.; Li, Q.; Xin, B.; Yao, T.; Wu, J. Construction of phosphorus-doped carbon nitride/phosphorus and sulfur co-doped carbon nitride isotype heterojunction and their enhanced photoactivity. *J. Colloid Interface Sci.* **2020**, *566*, 495–504. [CrossRef]

161. Liu, Q.; Shen, J.; Yu, X.; Yang, X.; Liu, W.; Yang, J.; Tang, H.; Xu, H.; Li, H.; Li, Y. Unveiling the origin of boosted photocatalytic hydrogen evolution in simultaneously (S, P, O)-Codoped and exfoliated ultrathin g-C$_3$N$_4$ nanosheets. *Appl. Catal. B Environ.* **2019**, *248*, 84–94. [CrossRef]

162. Jiang, L.; Guo, Y.; Pan, J.; Zhao, J.; Ling, Y.; Xie, Y.; Zhou, Y.; Zhao, J. N, P, O co-doped carbon filling into carbon nitride microtubes to promote photocatalytic hydrogen production. *Sci. Total Environ.* **2022**, *809*, 151114. [CrossRef]

163. Li, Y.; Li, X.; Zhang, H.; Xiang, Q. Porous graphitic carbon nitride for solar photocatalytic applications. *Nanoscale Horiz.* **2020**, *5*, 765–786. [CrossRef] [PubMed]

164. Eid, K.; Sliem, M.H.; Abdullah, A.M. Unraveling template-free fabrication of carbon nitride nanorods codoped with Pt and Pd for efficient electrochemical and photoelectrochemical carbon monoxide oxidation at room temperature. *Nanoscale* **2019**, *11*, 11755–11764. [CrossRef] [PubMed]

165. Eid, K.; Sliem, M.H.; Abdullah, A.M. Tailoring the defects of sub-100 nm multipodal titanium nitride/oxynitride nanotubes for efficient water splitting performance. *Nanoscale Adv.* **2021**, *3*, 5016–5026. [CrossRef] [PubMed]

166. Eid, K.; Soliman, K.A.; Abdulmalik, D.; Mitoraj, D.; Sleim, M.H.; Liedke, M.O.; El-Sayed, H.A.; AlJaber, A.S.; Al-Qaradawi, I.Y.; Reyes, O.M. Tailored fabrication of iridium nanoparticle-sensitized titanium oxynitride nanotubes for solar-driven water splitting: Experimental insights on the photocatalytic–activity–defects relationship. *Catal. Sci. Technol.* **2020**, *10*, 801–809. [CrossRef]

167. Abualrejal, M.M.; Eid, K.; Tian, R.; Liu, L.; Chen, H.; Abdullah, A.M.; Wang, Z. Rational synthesis of three-dimensional core–double shell upconversion nanodendrites with ultrabright luminescence for bioimaging application. *Chem. Sci.* **2019**, *10*, 7591–7599. [CrossRef] [PubMed]

168. Wu, F.; Eid, K.; Abdullah, A.M.; Niu, W.; Wang, C.; Lan, Y.; Elzatahry, A.A.; Xu, G. Unveiling one-pot template-free fabrication of exquisite multidimensional PtNi multicube nanoarchitectonics for the efficient electrochemical oxidation of ethanol and methanol with a great tolerance for CO. *ACS Appl. Mater. Interfaces* **2020**, *12*, 31309–31318. [CrossRef]

169. Ibrahim, Y.; Meslam, M.; Eid, K.; Salah, B.; Abdullah, A.M.; Ozoemena, K.I.; Elzatahry, A.; Sharaf, M.A.; Sillanpää, M. A review of MXenes as emergent materials for dye removal from wastewater. *Sep. Purif. Technol.* **2022**, *282*, 120083. [CrossRef]

170. Salah, B.; Eid, K.; Abdelgwad, A.M.; Ibrahim, Y.; Abdullah, A.M.; Hassan, M.K.; Ozoemena, K.I. Titanium Carbide (Ti$_3$C$_2$T$_x$) MXene Ornamented with Palladium Nanoparticles for Electrochemical CO Oxidation. *Electroanalysis* **2022**, *34*, 677–683. [CrossRef]

171. Ibrahim, Y.; Mohamed, A.; Abdelgawad, A.M.; Eid, K.; Abdullah, A.M.; Elzatahry, A. The recent advances in the mechanical properties of self-standing two-dimensional MXene-based nanostructures: Deep insights into the supercapacitor. *Nanomaterials* **2020**, *10*, 1916. [CrossRef]

172. Ibrahim, Y.; Kassab, A.; Eid, K.; Abdullah, A.M.; Ozoemena, K.I.; Elzatahry, A. Unveiling fabrication and environmental remediation of MXene-based nanoarchitectures in toxic metals removal from wastewater: Strategy and mechanism. *Nanomaterials* **2020**, *10*, 885. [CrossRef]

173. Ipadeola, A.K.; Eid, K.; Abdullah, A.M.; Al-Hajri, R.S.; Ozoemena, K.I. Pd/Ni-metal–organic framework-derived porous carbon nanosheets for efficient CO oxidation over a wide pH range. *Nanoscale Adv.* **2022**, *4*, 5044–5055. [CrossRef]

174. Ipadeola, A.K.; Eid, K.; Abdullah, A.M.; Ozoemena, K.I. Pd-Nanoparticles Embedded Metal–Organic Framework-Derived Hierarchical Porous Carbon Nanosheets as Efficient Electrocatalysts for Carbon Monoxide Oxidation in Different Electrolytes. *Langmuir* **2022**, *38*, 11109–11120. [CrossRef] [PubMed]

175. Nemati, F.; Rezaie, M.; Tabesh, H.; Eid, K.; Xu, G.; Ganjali, M.R.; Hosseini, M.; Karaman, C.; Erk, N.; Show, P.-L. Cerium functionalized graphene nano-structures and their applications; A review. *Environ. Res.* **2022**, *208*, 112685. [CrossRef] [PubMed]

176. Zhao, J.; Chen, Z.; Zhao, J. Metal-free graphdiyne doped with sp-hybridized boron and nitrogen atoms at acetylenic sites for high-efficiency electroreduction of CO$_2$ to CH$_4$ and C$_2$H$_4$. *J. Mater. Chem. A* **2019**, *7*, 4026–4035. [CrossRef]